

# Improving the Acidic Stability of Zeolitic Imidazolate Frameworks by Biofunctional Molecules

Song Gao,<sup>1</sup>Jingwei Hou,<sup>1,2,9,10,\*</sup> Zeyu Deng,<sup>2</sup>Tiesheng Wang,<sup>2</sup>Sebastian Beyer,<sup>3</sup>Ana Guilherme Buzanich,<sup>3</sup>Joseph J. Richardson,<sup>4</sup>Aditya Rawal,<sup>5</sup>Robert Seidel,<sup>6</sup>Muhammad Yazid Zulkifli,<sup>1</sup>Weiwei Li,<sup>2</sup>Thomas D. Bennett,<sup>2</sup>Anthony K. Cheetham,<sup>2</sup>Kang Liang,<sup>1,7,\*</sup> and Vicki Chen<sup>1,8</sup>

<sup>1</sup>School of Chemical Engineering, University of New South Wales, Sydney, NSW 2052, Australia

<sup>2</sup>Department of Materials Science and Metallurgy, University of Cambridge, Cambridge CB3 0FS, UK

<sup>3</sup>Federal Institute for Materials Research and Testing (BAM), Berlin 12205, Germany

<sup>4</sup>ARC Centre of Excellence in Convergent Bio-Nano Science and Technology and the Department of Chemical Engineering, The University of Melbourne, Parkville, VIC 3010, Australia

<sup>5</sup>Nuclear Magnetic Resonance Facility, Mark Wainwright Analytical Centre, University of New South Wales, Sydney, NSW 2052, Australia

<sup>6</sup>Helmholtz-Zentrum Berlin for Materials and Energy, Berlin 14109, Germany

<sup>7</sup>Graduate School of Biomedical Engineering, and Australian Centre for NanoMedicine, University of New South Wales, Sydney, NSW 2052, Australia

<sup>8</sup>School of Chemical Engineering, University of Queensland, St. Lucia, Brisbane, QLD 4072, Australia

<sup>9</sup>Present address: School of Chemical Engineering, University of Queensland, St. Lucia, Brisbane, QLD 4072, Australia

<sup>10</sup>Lead Contact

## SUMMARY

Zeolitic imidazolate frameworks (ZIFs) have been widely investigated for their use in separation, gas adsorption, catalysis, and biotechnology. Their practical applications, however, can be hampered by their structural instability in humid acidic conditions. Here, guided by density functional theory calculations, we demonstrate that the acidic stability of two polymorphic ZIFs (i.e., ZIF-8 and ZIF-L) can be enhanced by the incorporation of functional groups on polypeptides or DNA. A range of complementary synchrotron investigations into the local chemical structure and bonding environment suggest that the enhanced acidic stability arises from the newly established coordinative interactions between the Zn centers and the inserted carboxylate (for polypeptides) or phosphate (for DNA) groups, both of which have lower pK<sub>a</sub>s than the imidazolate ligand. With functional biomolecular homologs (i.e., enzymes), we demonstrate a symbiotic stability reinforcement effect, i.e., the encapsulated biomolecules stabilize the ZIF matrix while the ZIF exoskeleton protects the enzyme from denaturation.

## INTRODUCTION

Metal-organic frameworks (MOFs), an important category of porous materials, have attracted wide interest because of their flexibility in constructing various functional structures with precise molecular geometries.<sup>1</sup> Such properties make them promising candidates for various applications, including supercapacitors,<sup>2</sup> gas separations,<sup>3</sup> biopharmaceutical delivery,<sup>4,5</sup> and heterogeneous catalysis.<sup>6</sup> An emerging area of application is using MOFs as exoskeletons to protect vulnerable bioentities via pore entrapment or in situ encapsulation.<sup>7</sup> The former approach utilizes MOFs with inherent mesoporous structures or those in which mesoporous have been introduced via controlled etching.<sup>8–10</sup> On the other hand, the latter approach of in situ encapsulation allows microporous MOFs to be crystallized from precursors on the surface of bioentities. This enables the host of differently sized biomacromolecules and even living cells as well as more selective mass transfer via accessible micropores.<sup>5,11,12</sup> Among the thousands of known MOFs, zeolitic imidazolate frameworks (ZIFs), built with tetrahedral metal ions (e.g., Zn and Co) and imidazolate-based organic ligands, have been extensively investigated for in situ co-precipitation because of their satisfactory biocompatibility and relatively mild synthesis conditions.<sup>13–16</sup>

However, because the chemical stability of ZIFs is essentially reliant on the strength of their metal-ligand coordination bonds (usually Zn–N), their widespread application (e.g., gas adsorption and separation or biocatalytic reaction) has been limited by their susceptibility to dissolution under acidic conditions.<sup>17–21</sup> Density functional theory (DFT) calculations combined with experimental investigations have recently helped to elucidate the mechanism of ZIF dissolution in acidic conditions. These studies revealed that dissolution involves insertion of a water or acidic molecule into the Zn–N bond, followed by the subsequent dissociation of the protonated imidazole ligand away from the framework structure.<sup>22–24</sup> Topology, or network architecture, is important in controlling dissolution rates. For example, the {100} crystallographic facet of zeolitic imidazolate framework-8 (ZIF-8) is less susceptible to protonation over its {110} counterpart, despite the latter being more thermodynamically stable.<sup>23</sup> Through a statistical correlation of the dissolution rate constant with the chemical and structural properties of different ZIFs, a recent study revealed strong negative proportional correlations between the dissolution rate under humid acid exposure and both organic linker K<sub>a</sub> and ZIF hydrophilicity.<sup>22</sup> As a result, it is of great scientific and practical significance to explore the feasibility of improving the chemical stability of ZIFs by partially replacing imidazolate linkers of the “perfect” Zn–N tetrahedron with functional groups with higher pK<sub>a</sub> values. Defect engineering has been reported in the past as a method of tuning the stability of a variety of “pristine” MOFs,<sup>25</sup> but here, we concentrate on the potential to increase the chemical stability of ZIFs. Recent studies, from other researchers and ourselves, have established that certain functional biomolecules can rapidly induce the crystallization of ZIFs in aqueous solutions, which suggests

specific interactions arise between the biomolecules and the ZIF building blocks.<sup>5,26–28</sup> Specifically, a wide selection of amino acids have been observed to rapidly induce the formation of ZIFs in aqueous conditions—the major chemical similarity between them being the presence of amine and carboxylic acid, functional groups on the N and C termini, respectively.<sup>29</sup> We hypothesized that the interactions with these chemical groups could be utilized to fine-tune the physicochemical properties of ZIF-based biocomposites and, specifically, that molecules with a  $pK_a$  lower than the organic ligand (e.g., 2-methylimidazole or 2-Melm,  $pK_a = 7.86$ ) can coordinate with Zn nodes to stabilize the metal-organic complexes across a wider pH range. We therefore first performed DFT calculations to assess the viability of incorporating carboxylate groups (stronger Brønsted acids, with accordingly lower  $pK_a$ s than 2-Melm) onto the Zn–N tetrahedron to promote the chemical stability of the Zn–2-Melm complex (see Experimental Procedures). DFT results revealed that carboxylate groups increase the bonding strength of Zn–N by 27.82 kJ/mol during the acid-induced bond cleavage process (Figure 1A,  $\Delta E_{\text{break}}$  of the red Zn–N bond). This motivated us to study ZIF composites synthesized with a carboxylate group containing biomolecules for enhanced chemical stability (i.e., acid resistance).

In this study, we experimentally explored the feasibility of tuning the  $ZnN_4$  bonding environment by introducing functional groups in order to improve the acid stability of ZIFs. Two ZIF polymorphs were investigated, i.e., ZIF-L and ZIF-8. Both consist of Zn and 2-Melm building units. ZIF-L is a two-dimensional ZIF crystallizing in the orthorhombic space group Cmce. The Zn node contains a free dangling monodentate 2-Melm group, making it more susceptible to ligand replacement compared with ZIF-8, where all  $Zn_{2+}$  centers (surface groups aside) are connected to bidentate 2-Melm ligands.<sup>30</sup> Initially, two simple polypeptides, poly-L-glutamic acid (PGA,  $pK_a$  4.9, MW 45 kDa unless otherwise stated) and poly-L-lysine (PLL,  $pK_a$  9.4), containing carboxylate groups and amine groups, respectively, were employed (Figure 1B). To achieve a high and continuous density of carboxylic acid groups throughout the crystal, PGA was mixed with the ZIF precursor solution to induce the in situ formation of PGA@ZIF-L (Figure 1C) and PGA@ZIF-8 composites. As a benchmark, PLL composed solely of amine side groups was used to confirm that the carboxylate groups themselves were crucial for stabilization rather than the amines or hydrogen bonding amides in the polypeptide end group and backbone, respectively. A range of complementary characterization techniques, including solid-state nuclear magnetic resonance (NMR), X-ray photoelectron spectroscopy (XPS), synchrotron terahertz infrared spectroscopy (THz-FIR), small angle X-ray scattering (SAXS) and X-ray absorption fine structure spectroscopy (XAFS), were used to reveal the specific interactions between PGA and ZIF molecules, responsible for the improved acid stability. This improvement was more pronounced for PGA@ZIF-L than for the PGA@ZIF-8 composite. We further demonstrated the potential to improve the framework stability by incorporating more complex biomolecules, e.g., DNA and enzymes. Our results finally revealed that there exists a symbiotic stability reinforcement where the ZIFs exoskeleton not only protects the biomolecules from denaturation under harsh conditions but also is endowed with enhanced acid resistance as a result of the aforementioned interactions.

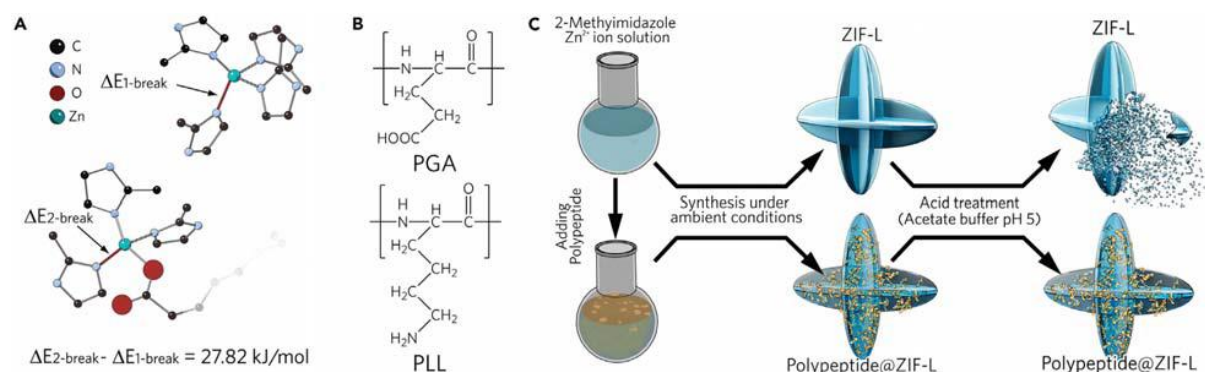


Figure 1. Conceptual Design to Improve the Acid Stability of ZIFs through the Synthesis of Polypeptide@ZIF-L Composites

(A) DFT calculation for the Zn–N bond strength variance after incorporating carboxylate group into the  $ZnN_4$  tetrahedron.

(B) Molecular structure of the PGA and PLL.

(C) Schematic illustration of the construction of ZIF-L and polypeptide@ZIF-L composites toward an improved acidic stability.

## RESULTS

### Assessing Chemical Structure and Bonding Environment of Polypeptide@ZIF-L

PGA@ZIF-L particles were synthesized via an aqueous-based approach involving the in situ nucleation of ZIF crystals from a solution of  $Zn(NO_3)_2$  and 2-Melm around PGA (Figures 1B and 1C). To remove the loosely attached PGA on the surface, the resultant PGA@ZIF-L particles were rinsed three times with Milli-Q water, and finally, the Bradford method (Table S1) was used to determine that over 98% of the added PGA was encapsulated within the PGA@ZIF-L. Synchrotron XAFS results of PGA@ZIF-L showed a reduced valence state of the Zn ions, suggesting a loss of coordination regularity in the first coordination shell around Zn (Figure S1A). This result suggested the successful incorporation of PGA within the ZIF-L molecular structure and that its presence may disrupt the original Zn–Melm tetrahedron arrangement, possibly because of the higher steric hindrance from the bulky PGA molecules. The results of Fourier transformed (FT) extended X-ray absorption fine structure (EXAFS; Figure S1B) suggested that the overall ZIF-L structure was intact after the incorporation of PGA. The above results were in line with the solid-state <sup>13</sup>C NMR spectrum of the PGA@ZIF-L (Figure 2A), where the sharp well-resolved <sup>13</sup>C NMR signals of the 2-Melm ligand are consistent with the ZIF-L structure.<sup>30</sup> The signature <sup>13</sup>C NMR peaks originating from PGA can be observed in the composite samples and were low in intensity and significantly broadened compared to the 2-Melm peaks (the PGA peaks are replotted in the insets with a 20-fold vertical expansion; more details can be

found in the Experimental Procedures). The  $^{13}\text{C}\{^1\text{H}\}$  two-dimensional HETCOR correlating the  $^{13}\text{C}$  and  $^1\text{H}$  species for the PGA@ZIF-L composite (Figures 2B and S2) demonstrated an intermolecular correlation signal between the PGA N-C-H species and the 2-Melm- $\text{CH}_3$  species, providing cooperative evidence that the PGA was embedded in the ZIF-L crystals. The dashed red lines indicate the intramolecular correlation signals of the different 2-Melm  $^1\text{H}$  species with the methyl  $^{13}\text{C}$  species. The dashed green line indicates the intermolecular correlation peak between the PGL N-C-H species and the imidazole methyl species. The polarization transfer confirms a nanometer-scale proximity between the PGA and ZIF-L. In addition, SAXS diffraction patterns (Figure S3) and the  $^{13}\text{C}$  NMR spectrum both highlighted that the crystal structure of ZIF-L was well preserved after incorporating PGA. The BET surface area decreased by  $\sim 30\%$  (from 1,419 to 981  $\text{m}^2/\text{g}$ ) because of the added mass of the polypeptide and potentially also because of the partial occupation of the open ZIF pores or pore blocking by the polypeptides (Figure S4).

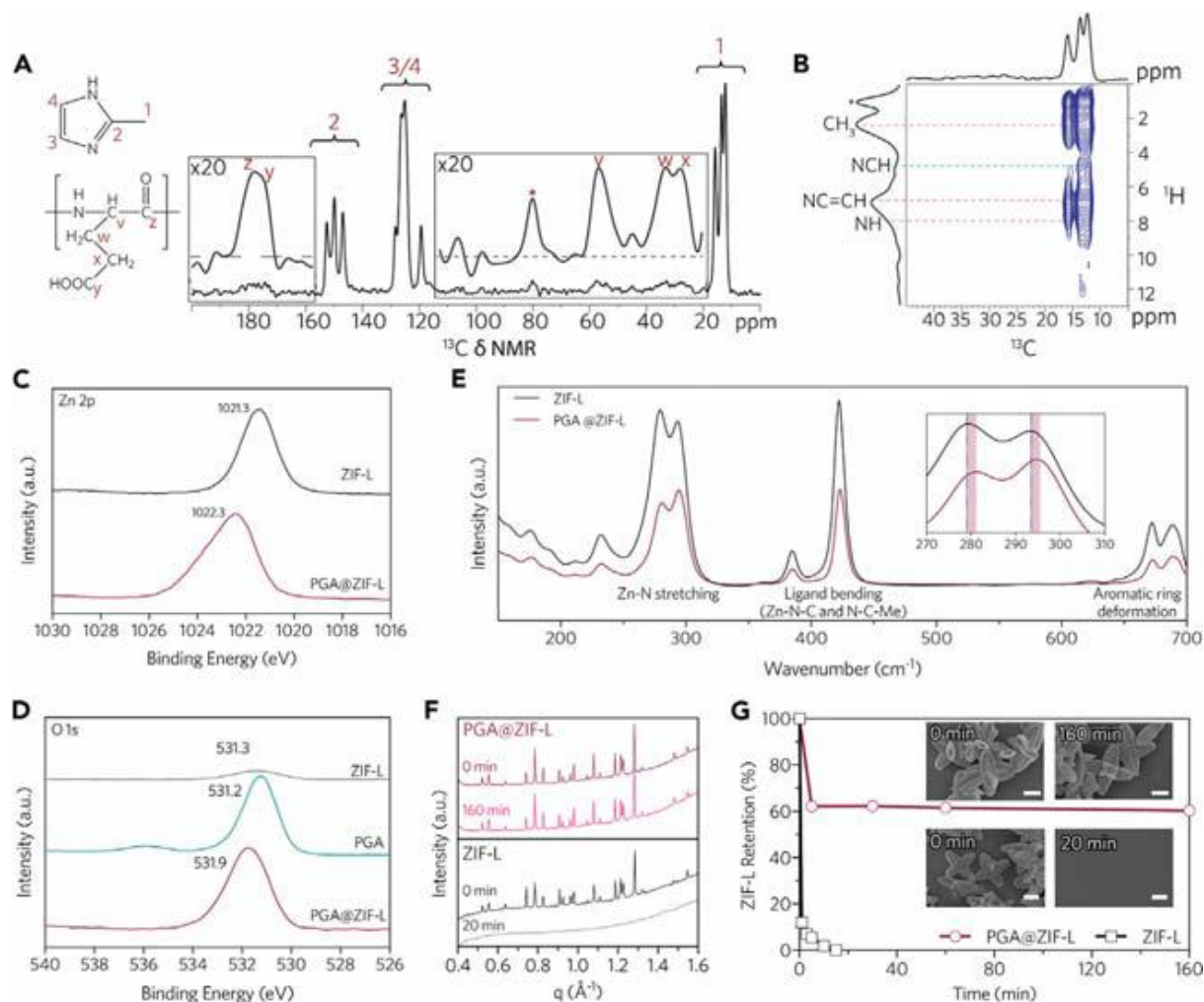


**Figure 2. Change in Coordination for ZIF-L after PGA Incorporation and Stability of PGA@ZIF-L in Acidic Conditions**

(A) One-dimensional  $^{13}\text{C}$  NMR results of the PGA@ZIF-L, along with peak assignments. The signals of the PGA moieties are plotted in the insets with a 203

vertical magnification and a stronger line broadening to better suppress the noise with the dashed line indicating zero intensity.

(B) Two-dimensional  $^{13}\text{C}\{^1\text{H}\}$  HETCOR for the PGA@ZIF-L system. The one-dimensional  $^{13}\text{C}$  and  $^1\text{H}$  projections are plotted at the top and left, respectively. The peaks marked with \* are the zero-frequency artifacts.

(C and D) XPS Zn 2p (C) and O 1s (D) spectra of the PGA@ZIF-L (red), PGA (green), and ZIF-L (black).

(E) THz-FIR spectroscopy of ZIF-L (black) and PGA@ZIF-L (red).

(F) SAXS diffraction patterns for PGA@ZIF-L and ZIF-L during the acid dissolution process in acetate buffer (50 mM, pH 5).

(G) ZIF-L retention based on monitoring the Zn ions in solution by ICP-MS for PGA@ZIF-L (red) and pure ZIF-L (black). Insets show SEM images for PGA@ZIF-L and ZIF-L at the beginning and end of their respective dissolution tests. Scale bars represent 1  $\mu\text{m}$ .

The elemental surveys from XPS (Figures 2C, 2D, and S5) revealed that after the incorporation of PGA, the Zn 2p and O 1s core-levels both shift toward higher binding energies, consistent with the formation of new coordination bonds, between Zn and O. This leads to a higher energy barrier to protonation for the Zn–N bonds.<sup>31</sup> In addition, as characterized by synchrotron far-infrared (FIR)-terahertz (THz) radiation (Figures 2E and S6), the presence of PGA led to a blue shift of the Zn–N stretching peaks at 168, 278, and 293  $\text{cm}^{-1}$  (in ZIF-L) by 3  $\text{cm}^{-1}$ , which aligned with the anticipated bond strength enhancement based on DFT.<sup>32,33</sup> It should be noted that the presence of two Zn–N peaks originates from the in-plane dual-coordinated and the out-of-plane dangling 2-Melm ligands in ZIF-L, respectively. These results were confirmed by Fourier transform infrared spectroscopy (FTIR), where proposed Zn-carboxylate interactions were confirmed by the blue-shifted C=O peak on PGA (Figure S7).<sup>34,35</sup> Thus, both the experimental and DFT results supported our hypothesis that carboxylate groups interact with Zn centers in the polypeptide@ZIFs composites.

### Effect of Polypeptides on ZIF-L and ZIF-8 Acid Stabilization

We next investigated whether the Zn-carboxylate interactions could alter the chemical stability of ZIFs. The effect of PGA on the acid stability of ZIF-L was explored by soaking both ZIF-L and PGA@ZIF-L in acetate buffer (50 mM, pH 5). We found that PGA@ZIF-L was significantly more resistant to acid than the pure ZIF-L. For example, the characteristic peaks belonging to pure ZIF-L completely disappeared in the SAXS pattern after being subjected to acidic conditions for 20 min, whereas PGA@ZIF-L was able to maintain both its diffraction and porosity after an extended period of treatment of nearly 3 h (Figures 2F and S8). Inductively coupled plasma mass spectroscopy (ICP-MS) analysis of the dissolved Zn<sup>2+</sup> in solution indicated that over 60% of the PGA@ZIF-L can be preserved against dissolution even after 3 h of soaking in acidic conditions (50 mM acetate buffer, pH 5), as compared with the complete dissolution of pure ZIF-L after 20 min (Figures 2G and S9). The corresponding SEM images confirmed that PGA@ZIF-L could maintain its original morphological features after acid treatment, other than small changes at particle edges. In addition, better acid stability of PGA@ZIF-L can be achieved when higher molecular weights of PGA (1.5, 15, and 45 kDa, 0.22 mmol) are encapsulated within ZIF-L (Figure S10). To confirm the importance of the carboxylate groups of PGA on the acidic stability of ZIF-L, rather than the N and C termini or polypeptide backbone, we replaced PGA with PLL (Figure 1B), which has an abundance of primary amine groups but no carboxylate groups (except the C-terminal carboxylate). No obvious change in acid stability from pure ZIF-L benchmark was observed for the PLL@ZIF-L composite (Figure S11), even though newly formed coordination bonds between the primary amines of PLL and Zn centers are formed, as determined by XPS, XAFS, THz FIR, solid-state NMR, and FTIR (Figures S12–S15; Table S1). These results further support our hypothesis that the Brønsted acidity (pK<sub>a</sub>) of the interacting group is crucial for tuning the acid stability of ZIFs. Specifically, a pK<sub>a</sub> above that of 2-Melm reduces acid stability and a pK<sub>a</sub> below that of 2-Melm improves the acid stability of the final ZIF structure. Additionally, the comparison between PGA and PLL allowed us to rule out other factors that could lead to better acid stability, such as (1) pore blockage, (2) hydrogen bonding by the peptide backbone, and (3) hydrophilic effects by the side groups.<sup>22</sup>

It is worth noting that although the improved stability of the ZIF originates from the coordination bonds between low pK<sub>a</sub> groups (e.g., carboxylate) and Zn, when PGA was encapsulated within ZIF-8 (PGA@ZIF-8), the stabilization effect was less pronounced compared with ZIF-L counterparts (Table S1; Figure S16). Although both ZIF-L and ZIF-8 share the same type of coordination bonds and organic linkers, the structural arrangement of 2-Melm around the metal center is different. The <sup>13</sup>C NMR indicates the presence of three distinct environments for the 2-Melm moiety in ZIF-L (Figure 2A), compared with a single environment in ZIF-8 (Figure S17). More specifically, while the 2-Melm ligand is bidentate in ZIF-8, the co-existence of bidentate, monodentate, and free 2-Melm was observed for ZIF-L.<sup>36</sup> Therefore, the difference in the interaction with guest molecules can be expected for the two types of frameworks.

The in situ encapsulation applied in this work is a kinetically driven process; therefore, the presence of excessive 2-Melm in the ZIF-8 precursor solution could compete with the carboxylate groups on biomolecules to form bonding with Zn nodes, which leads to overall weaker interaction between carboxylate groups and Zn (Figures S18 and S19, FT-IR and XPS results). Particularly, the split peaks at 282 and 292 cm<sup>-1</sup> in THz-FIR spectrum for the PGA@ZIF-8 composite (Figure S20) suggests even though Zn–N bond strength enhancement has been confirmed, a large amount of the original Zn–Melm tetrahedron bonding environment is still invariant, which explains the limited stability enhancement for ZIF-8 system. In comparison, ZIF-L is synthesized with a lower 2-Melm to Zn molar ratio, which is beneficial to generate Zn–O bonding with the carboxylate on biomolecules and thus contributes to the improved acid resistance.<sup>36–39</sup> Differences may also possibly be ascribed to the greater accessibility of Zn sites in the two-dimensional ZIF-L structure, as opposed to the three-dimensional ZIF-8 structure.

### Effect of DNA on ZIF-L Acid Stabilization

To expand the versatility of this concept and further confirm that the lower pK<sub>a</sub> of the carboxylate groups of PGA is responsible for the enhanced acid stability, we synthesized ZIF-L with a biomolecule containing phosphate (pK<sub>a</sub> ~0) groups in its backbone, namely DNA (Figure 3A). The DNA@ZIF-L material still contained the inherent ZIF-L crystal structure (Figure S21; Table S2), and the cross-sectional SEM image after removing DNA by calcination (Figure S22) suggests that the DNA is evenly distributed within the ZIF-L matrix. The two-dimensional HETCOR (Figure 3B) shows the intra-molecular correlation signals of the DNA sugar and base <sup>1</sup>H species with the phosphate group. Importantly, there is also a distinct correlation signal to <sup>1</sup>H methyl species at ~2 ppm, which appears as a shoulder next to the sugar correlation peak. Since the CH<sub>3</sub> species belong to the 2-Melm, the experiment establishes that there is a close proximity between the DNA and ZIF-L. Within the context of the present system, the <sup>31</sup>P–CH<sub>3</sub> correlation signal establishes that the DNA is encapsulated into the ZIF-L and not simply adsorbed onto the surface. Since the ZIF-L particle size is of the order of microns, their specific external surface area is very low. As a result, the signal of the DNA specifically adsorbed on the external surface would be undetectable because of the inherently low sensitivity of NMR spectroscopy. The only way DNA would have sufficient molecular contact with the methylimidazolate ligand for detection via NMR is if the DNA were encapsulated into the interior structure of the ZIF-L. From the two-dimensional HETCOR results, it also should be noted that the CH<sub>3</sub> signal from 2-Melm is smaller than the DNA signal, which indicates that the <sup>1</sup>H spin diffusion has not equilibrated and that the DNA is most likely present in a folded form rather than extended within the composite.<sup>40</sup> Because of the mild in situ co-precipitation conditions, the original B-type double-helix structure of DNA was well preserved after being encapsulated in ZIF-L as determined by circular dichroism (CD) spectroscopy (Figure S23).

ICP-MS, SEM, and X-ray diffraction (XRD) analyses suggest that the effect of DNA on ZIF-L stabilization in acidic conditions (50 mM acetate buffer, pH 5) is even more pronounced than having PGA in the framework (Figure 3C), and the ZIF-L crystallinity was preserved after 160 min (Figure S24). These results point toward stronger interactions between ZIF-L and DNA because of the lower pK<sub>a</sub> of the phosphate groups in the DNA backbone than the carboxylate groups of PGA. Further characterization results obtained from synchrotron XAFS, XPS, and synchrotron liquid jet XPS confirmed the emergence of bonding for Zn ions–DNA (phosphate acid coordination with Zn nodes), as well as 2-Melm–DNA (Figures S25–S27). In combination with the PGA data, this confirms that the pK<sub>a</sub> of the interacting group is crucial for improving the acid stability of ZIF-L. Moreover, this shows that the stability improvement from polypeptide and DNA incorporation allows us to exploit more complex, functional biomacromolecules possessing similar chemical groups.

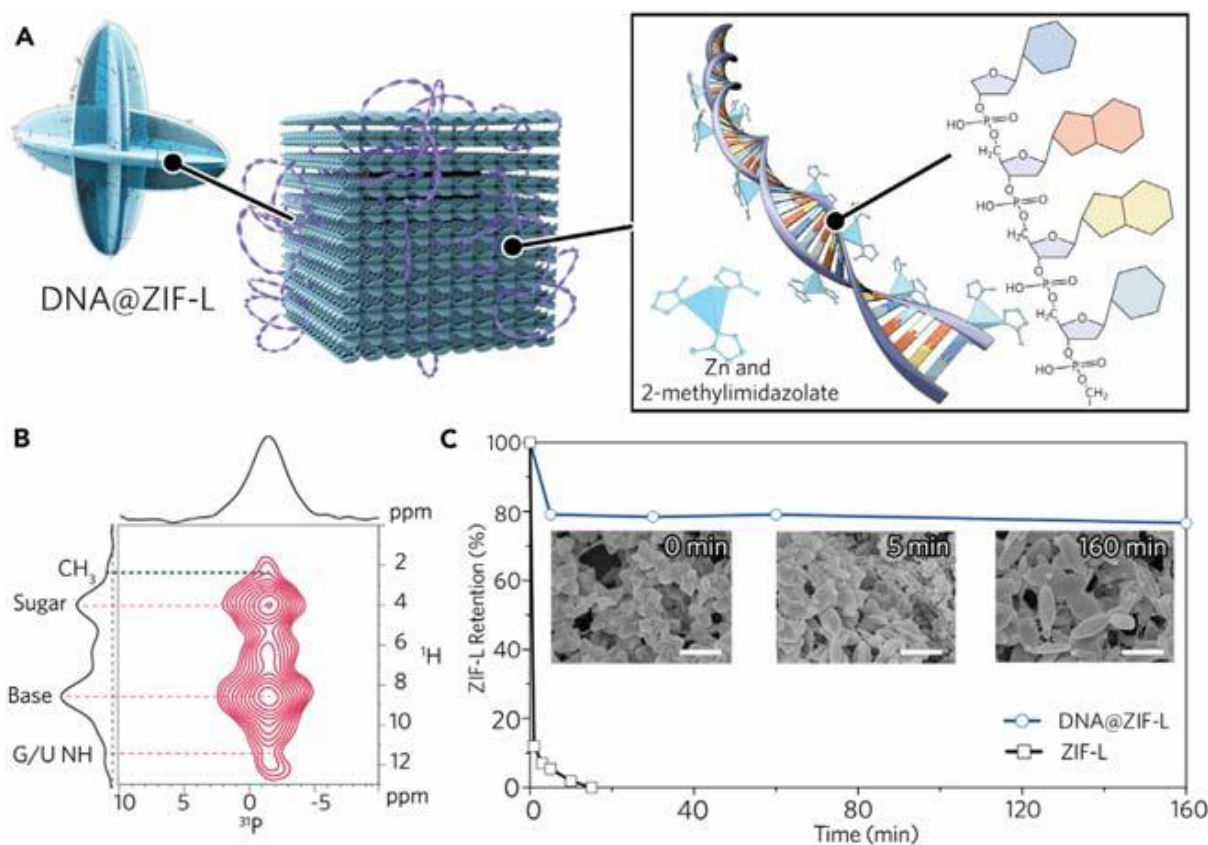


Figure 3. Improved Acidic Stability for DNA@ZIF-L Composites

(A) Schematic diagram of the DNA@ZIF-L.

(B) Two-dimensional  $^{31}\text{P}\{^1\text{H}\}$  HETCOR for the DNA@ZIF-L system. The one-dimensional  $^{31}\text{P}$  and  $^1\text{H}$  projections are plotted at the top and left, respectively.

(C) ZIF-L retention based on monitoring the Zn ions in solution by ICP-MS for DNA@ZIF-L (blue) and pure ZIF-L (black). Insets show SEM images for DNA@ZIF-L during the acid treatment process. Scale bars represent 2 mm.

### Symbiotic Stability Reinforcement between Enzymes and ZIF-L

Enzyme encapsulation in MOFs represents an emerging branch of science because of the excellent protection of vulnerable biomolecules and the controlled transportation of substrates for biocatalysis offered by the porous MOFs.<sup>12–16,41–43</sup> Therefore, we next investigated whether complex functional biomolecules, i.e., enzymes, could be used to enhance the acid stability of ZIFs and whether the ZIFs simultaneously protect the enzyme against harsh conditions (i.e., high temperature). Although extensive research has been focused on employing MOF coatings to enhance biomolecular stability, it has not yet been demonstrated that the functional bioentities can contribute any enhanced stability back to the MOFs. Many enzymes, e.g., catalase, have surface accessible carboxylate groups identical to PGA,<sup>44,45</sup> and we therefore investigated whether these carboxylate groups could play a role in protecting enzyme@ZIF-L composites from dissolution in acidic conditions. As a demonstration, we immobilized catalase in ZIF-L (catalase@ZIF-L; Figure 4A) and then used confocal laser scanning microscopy (CLSM) performed on fluorescein isothiocyanate (FITC)-labeled catalase (Figure 4B) to show that catalase was successfully and uniformly entrapped within the ZIF-L. Moreover, the original ZIF-L morphology and crystal structure were well preserved, as confirmed by transmission electron microscopy (TEM), dynamic light scattering (DLS), and SAXS measurements (Figures S28 and S29). The formation of a new coordination bond between Zn and O for catalase@ZIF-L was implied by the XPS peak shift of Zn (Figure S30), though it was less significant than PGA@ZIF-L. We exposed the catalase@ZIF-L to acidic conditions (pH 5, 50 mM acetate buffer) and confirmed its improved stability against acid (Figure 4C). Roughly 45% of the ZIF-L crystallinity was retained after acid treatment (150 min), which is slightly lower than the PGA@ZIF-L composite (~60%) (Figures S31 and S32), suggesting that not only is the  $\text{pK}_a$  of the groups important but so too is their density. To further explore the effect of the carboxylate group across different biomolecules, we encapsulated equal molar quantity (0.04 mmol) of 45 kDa PGA and catalase (containing ~306 and 256 carboxylate groups per molecule, respectively) within ZIF-L and observed comparable acid stability (Figure S33). However, it should be noted that the interaction between the framework and biomolecule is also determined by the shape, surface charge, and the presence of other functional groups on the biomolecules in addition to the number of carboxylate groups.

In addition to the improved stability of ZIF-L, the ZIF-L can also stabilize the incorporated catalase. Catalase converts  $\text{H}_2\text{O}_2$  to  $\text{H}_2\text{O}$  and  $\text{O}_2$ ,<sup>46</sup> and under ambient conditions, the catalase@ZIF-L exhibited a ~45% improved activity compared with an equivalent quantity of free catalase. Enzyme kinetic parameters (Table S3) confirmed the enhanced activity mainly originated from the improved affinity between the immobilized enzyme and substrate (as suggested by a lower  $K_m$ ), especially at the low  $\text{H}_2\text{O}_2$  concentration condition, though the turnover number ( $K_{\text{cat}}$ ) of the catalase experienced loss after immobilization because of the unfavorable hydrophobic interactions with the framework.<sup>47</sup> Further thermal (80 °C) or acid treatment (pH 5) revealed a significant improvement in the retained activity for the catalase@ZIF-L (Figure 4D) compared to free catalase. These results align with other enzyme@MOF work, where it

has been shown that MOFs can serve as porous selective concentrators for catalytic substrates, while also helping to preserve biomolecules from denaturation.<sup>19,26</sup> These experiments with functional enzymes highlight not only that the ZIF can protect the biomolecule but also that the biomolecule can stabilize the ZIF.

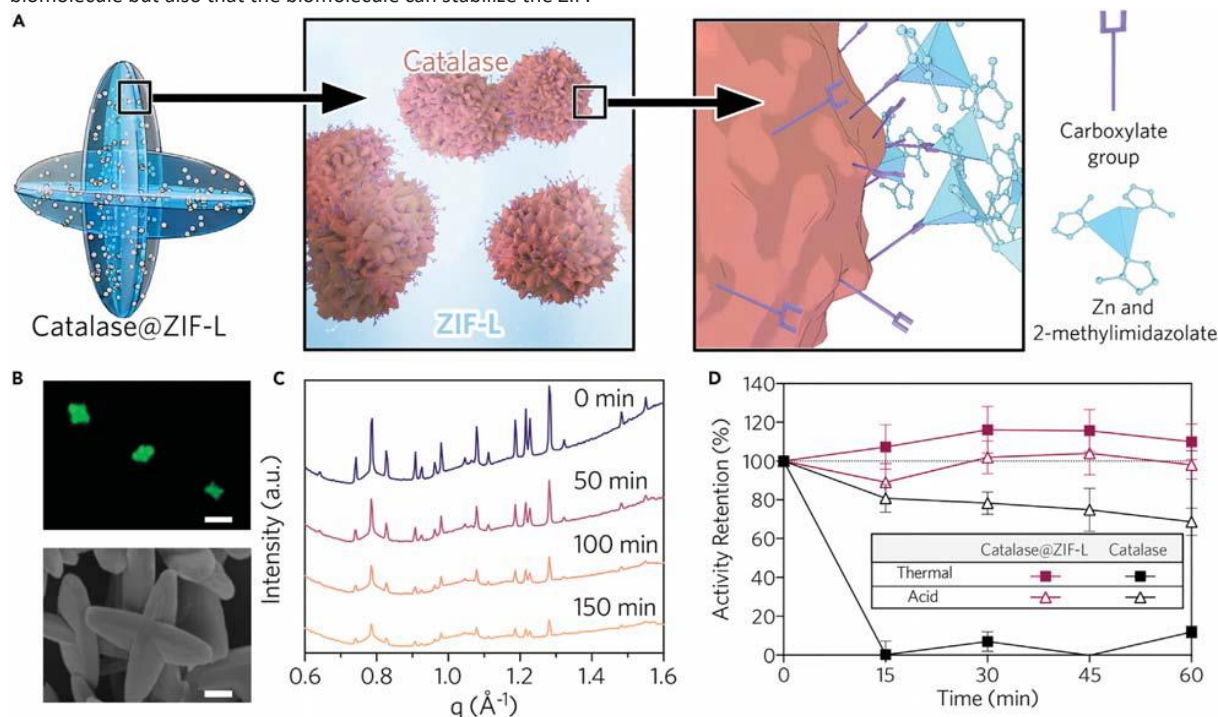


Figure 4. Structure, Morphology, and Stability Performance of the Catalase@ZIF-L Composites

(A) Schematic diagram of catalase@ZIF-L.

(B) CLSM and SEM images of the catalase@ZIF-L composite materials. Scale bars represent 5  $\mu\text{m}$  (CLSM) and 500 nm (SEM).

(C) In situ SAXS diffraction patterns for catalase@ZIF-L during acid treatment.

(D) Retention of the biocatalytic efficiency of catalase@ZIF-L with different treatment. Data are represented as three parallel tests.

## DISCUSSION

Enhancing MOF stability in aqueous conditions is essential for the realization of MOFs in the real world, as opposed to proof-of-concept applications, and therefore has been a major goal of recent research.<sup>48</sup> It can be achieved by tuning the chemical composition of the MOFs or by introducing an external protective layer coating. However, these are usually accompanied by a loss of porous structure or accessibility of the pores. One recent study applied a “sacrificial” bond to promote the hydrolytic stability of the copper-based MOFs, allowing the MOF to have excellent hydrolytic stability.<sup>49</sup> Our study uses biomolecules to promote the chemical stability of ZIFs through bonding interactions between biomolecules and  $\text{Zn}^{2+}$  centers. Specifically, guided by DFT calculations suggesting that the Zn–N bond strength can be improved after replacement of an imidazolate group by a carboxylate group in the Zn tetrahedral environment, we have demonstrated that the acid stability of ZIF-8 and particularly ZIF-L can be bolstered using biopolymers rich in functional groups with low  $\text{pK}_a$ s. We focused on polypeptides rich in carboxylic acid groups and DNA rich in phosphate groups to nucleate the ZIF-L growth in situ. Importantly, this strategy can also be applied to functional biomolecules such as enzymes. We demonstrated for the first time that there exists a symbiotic stability reinforcement between soft, flexible biomolecules (e.g., catalase) and rigid, crystalline ZIF-L, where not only the framework protects the biomolecules from denaturation in harsh conditions but also the biomolecule enhances the acid resistance of the MOF. We believe this approach may accelerate further developments of MOFs in biomedical technology, such as molecular protection, biocatalysis, drug delivery, and biosensing, by allowing us to tune the stability of MOF complexes. Moreover, such strategies provide a potential route for stabilizing MOFs that show promising characteristics for industrial and biological uses but are unstable in the wide range of environmental conditions experienced outside of the laboratory. Finally, it is foreseeable that this bonding environment regulating principle could be further expanded to polymer-MOF host-guest systems,<sup>50,51</sup> where polymers possessing certain functionalities are synthesized inside the MOFs in situ.

## EXPERIMENTAL PROCEDURES

### Synthesis of PGA/PLL/DNA/Catalase@ZIF-L

In a typical synthetic procedure, 1 mL of polypeptide-DNA-enzyme solution (10 mg/mL) was mixed with 10 mL of 2-Melm solution (0.8 M), to which was added 1 mL of zinc nitrate solution (0.5 M). The mixture solution was continuously stirred for 30 min. To separate the particles from the supernatant liquid, the resultant suspension solution was then centrifuged at 6,000 rpm for 10 min. Then, the particles were rinsed with Milli-Q water. The centrifugation-rinsing step was repeated three times to remove all unreacted chemicals. Finally, the particles were vacuum dried. Similar procedures were applied for the PGA@ZIF-8 synthesis, except for the concentrations of 2-Melm solution (5 mL) and zinc nitrate solution (5 mL) were 1.0 and 0.05 M, respectively. The amount of the

encapsulated biomolecules within ZIF-L and ZIF-8 was examined by the Bradford assay. In brief, for each test, 50.0 mL of the sample solution was mixed with 1.50 mL Bradford reagent at room temperature; then, the solution UV absorption was monitored at 595 nm and compared with standard samples with known concentrations. ZIFs Stability Test under Acidic Conditions A 0.5 mL suspension solution containing 5 mg ZIFs (or ZIF composites) was mixed with 3 mL of sodium acetate buffer (50 mM, pH 5). The degradation test was conducted under constant stirring at 100 rpm. The ZIF decomposition was monitored by SEM imaging and detecting the instant Zn ions concentration in the degraded solution. ZIF-L in acid suspension solution was collected at certain time intervals and immediately filtered through a 0.1 mm filter after dilution (the background adsorption of Zn by the filter was less than 0.5 %). After dilution, the permeate was digested and analyzed with the ICP-MS, which was performed on a PerkinElmer Optima DV7300 IPOES instrument.

## SUPPLEMENTAL INFORMATION

Supplemental Information can be found online at <https://doi.org/10.1016/j.chempr.2019.03.025>.

## ACKNOWLEDGMENTS

The authors thank the HZB staff for assistance during the beamtime at BESSY II. This work is supported under the Australian Research Council's Discovery Projects funding scheme (DP150104485 and DP180103874), the Australia National Health and Medical Research Council (NHMRC) Career Development Fellowship (APP1163786), and the UNSW Scientia Fellowship program (K.L.). A.K.C. thanks the Ras al Khaimah Centre for Advanced Materials for financial support. T.D.B. thanks the Royal Society for a university research fellowship (UF150021). Z.D. would like to thank the Cambridge Overseas Trust and the China Scholarship Council. DFT calculations were performed at the UK National Supercomputing Service, ARCHER. Access was obtained via the Materials Chemistry Consortium and funded by EPSRC under grant number EP/L000202/1. T.W. thanks the China Scholarship Council for funding and the EPSRC Centre for Doctoral Training in Sensor Technologies and Applications (EP/L015889/1 and 1566990) for support. R.S. thanks the German Research Foundation (DFG) for an Emmy-Noether Young Investigator stipend (SE 2253/3-1). S.B. thanks BAM for the postdoctoral Adolf Martens Fellowship. Part of this research was undertaken on the small-/wide-angle X-ray scattering and THz-Far-IR beamlines at the Australian Synchrotron, part of ANSTO. We acknowledge Helmholtz-Zentrum Berlin for the granted beamtime at the BAMline.

## AUTHOR CONTRIBUTIONS

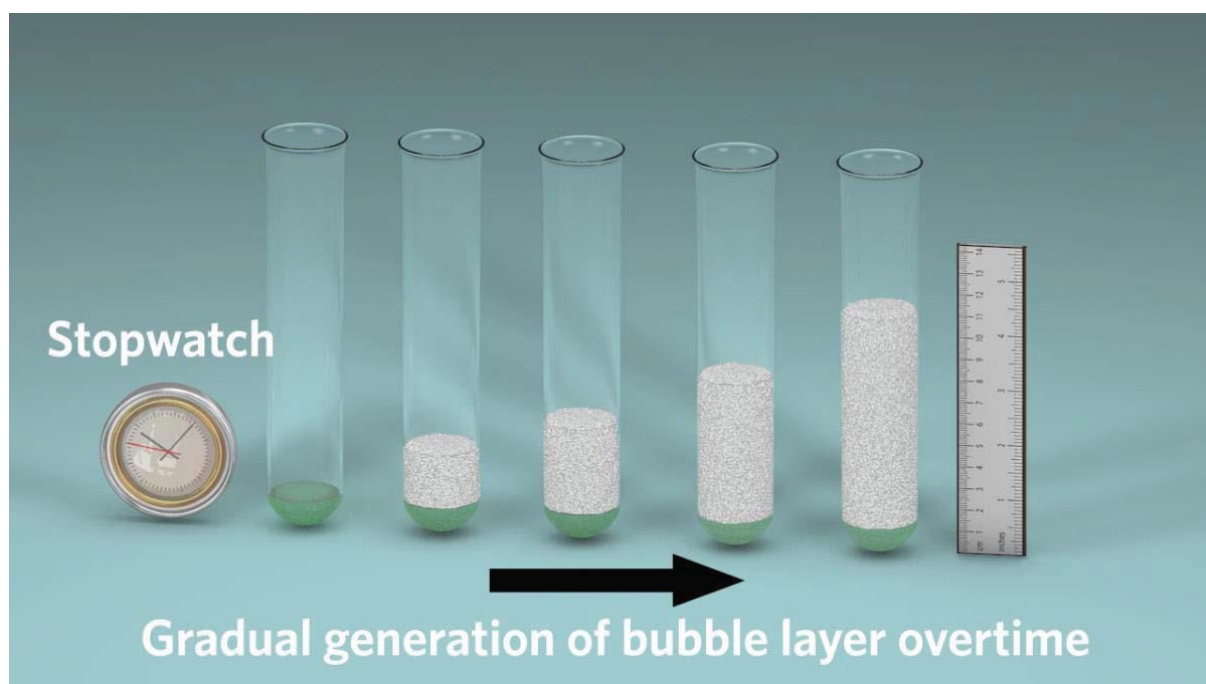
Conceptualization, S.G., J.H., and K.L.; Methodology, J.H. and T.W.; Investigation, S.G., J.H., J.R., W.L., Z.D., S.B., A.G.B., R.S., and A.R.; Writing – Original Draft, S.G., J.H., T.W., and K.L.; Writing – Review & Editing, A.R., A.K.C., T.D.B., and V.C.; Visualization, J.H.; Supervision, A.K.C., T.D.B., and V.C.; Funding Acquisition, K.L., T.D.B., and V.C.

## REFERENCES AND NOTES

1. Furukawa, H., Cordova, K.E., O'Keeffe, M., and Yaghi, O.M. (2013). The chemistry and applications of metal-organic frameworks. *Science* 341, 1230444.
2. Salunkhe, R.R., Young, C., Tang, J., Takei, T., Ide, Y., Kobayashi, N., and Yamauchi, Y. (2016). A high-performance supercapacitor cell based on ZIF-8-derived nanoporous carbon using an organic electrolyte. *Chem. Commun.* 52, 4764–4767.
3. Song, Q., Nataraj, S.K., Roussenova, M.V., Tan, J.C., Hughes, D.J., Li, W., Bourgoin, P., Alam, M.A., Cheetham, A.K., Al-Muhtaseb, S.A., et al. (2012). Zeolitic imidazolate framework (ZIF-8) based polymer nanocomposite membranes for gas separation. *Energy Environ. Sci.* 5, 8359–8369.
4. Jiang, J., Babarao, R., and Hu, Z. (2011). Molecular simulations for energy, environmental and pharmaceutical applications of nanoporous materials: from zeolites, metal-organic frameworks to protein crystals. *Chem. Soc. Rev.* 40, 3599–3612.
5. Liang, K., Ricco, R., Doherty, C.M., Styles, M.J., Bell, S., Kirby, N., Mudie, S., Haylock, D., Hill, A.J., Doonan, C.J., et al. (2015). Biomimetic mineralization of metal-organic frameworks as protective coatings for biomacromolecules. *Nat. Commun.* 6, 7240.
6. Wang, Z.J., Clary, K.N., Bergman, R.G., Raymond, K.N., and Toste, F.D. (2013). A supramolecular approach to combining enzymatic and transition metal catalysis. *Nat. Chem.* 5, 100–103.
7. Lian, X., Fang, Y., Joseph, E., Wang, Q., Li, J., Banerjee, S., Lollar, C., Wang, X., and Zhou, H.C. (2017). Enzyme-MOF (metal-organic framework) composites. *Chem. Soc. Rev.* 46, 3386–3401.
8. Li, P., Chen, Q., Wang, T.C., Vermeulen, N.A., Mehdi, B.L., Dohnalkova, A., Browning, N.D., Shen, D., Anderson, R., Go' mez-Gualdro' n, D.A., et al. (2018). Hierarchically engineered mesoporous metal-organic frameworks toward cell-free immobilized enzyme systems. *Chem* 4, 1022–1034.
9. Jeong, G.Y., Singh, A.K., Kim, M.G., Gyak, K.W., Ryu, U., Choi, K.M., and Kim, D.P. (2018). Metal-organic framework patterns and membranes with heterogeneous pores for flow-assisted switchable separations. *Nat. Commun.* 9, 3968.
10. Liang, W., Li, L., Hou, J., Shepherd, N.D., Bennett, T.D., D'Alessandro, D.M., and Chen, V. (2018). Linking defects, hierarchical porosity generation and desalination performance in metal-organic frameworks. *Chem. Sci.* 9, 3508–3516.
11. Liang, K., Richardson, J.J., Cui, J., Caruso, F., Doonan, C.J., and Falcaro, P. (2016). Metal-organic framework coatings as cytoprotective exoskeletons for living cells. *Adv. Mater.* 28, 7910–7914.
12. Chen, W.-H., Va' zquez-Gonza' lez, M., Zoabi, A., Abu-Reziq, R., and Willner, I. (2018). Biocatalytic cascades driven by enzymes encapsulated in metal-organic framework nanoparticles. *Nat. Catal.* 1, 689–695.
13. Liao, F.S., Lo, W.S., Hsu, Y.S., Wu, C.C., Wang, S.C., Shieh, F.K., Morabito, J.V., Chou, L.Y., Wu, K.C.-W., and Tsung, C.K. (2017). Shielding against unfolding by embedding enzymes in metal-organic frameworks via a de novo approach. *J. Am. Chem. Soc.* 139, 6530–6533.
14. Chu, Y., Hou, J., Boyer, C., Richardson, J.J., Liang, K., and Xu, J. (2018). Biomimetic synthesis of coordination network materials: Recent advances in MOFs and MPNs. *Appl. Mater.* Today 10, 93–105.
15. Lyu, F., Zhang, Y., Zare, R.N., Ge, J., and Liu, Z. (2014). One-pot synthesis of protein-embedded metal-organic frameworks with enhanced biological activities. *Nano Lett.* 14, 5761–5765.
16. Shieh, F.K., Wang, S.C., Yen, C.I., Wu, C.C., Dutta, S., Chou, L.Y., Morabito, J.V., Hu, P., Hsu, M.H., Wu, K.C.-W., et al. (2015). Imparting functionality to biocatalysts via embedding enzymes into nanoporous materials by a de novo approach: size-selective sheltering of catalase in metal-organic framework microcrystals. *J. Am. Chem. Soc.* 137, 4276–4279.

17. Zhuang, J., Kuo, C.H., Chou, L.Y., Liu, D.Y., Weerapana, E., and Tsung, C.K. (2014). Optimized metal–organic-framework nanospheres for drug delivery: evaluation of small-molecule encapsulation. *ACS Nano* 8, 2812–2819.
18. Avci, C., Arin<sup>ez</sup>-Soriano, J., Carne<sup>-Sa</sup> nchez, A., Guillerm, V., Carbonell, C., Imaz, I., and Maspocho, D. (2015). Post-synthetic anisotropic wet-chemical etching of colloidal sodalite zif crystals. *Angew. Chem. Int. Ed.* 54, 14417–14421.
19. Zhang, Y., Ge, J., and Liu, Z. (2015). Enhanced activity of immobilized or chemically modified enzymes. *ACS Catal.* 5, 4503–4513.
20. Park, K.S., Ni, Z., Co<sup>te</sup>, A.P., Choi, J.Y., Huang, R., Uribe-Romo, F.J., Chae, H.K., O’Keeffe, M., and Yaghi, O.M. (2006). Exceptional chemical and thermal stability of zeolitic imidazolate frameworks. *Proc. Natl. Acad. Sci. USA* 103, 10186–10191.
21. Yuan, S., Feng, L., Wang, K., Pang, J., Bosch, M., Lola, C., Sun, Y., Qin, J., Yang, X., Zhang, P., et al. (2018). Stable metal-organic frameworks: design, synthesis, and applications. *Adv. Mater.* 30, 1704303.
22. Bhattacharyya, S., Han, R., Kim, W.-G., Chiang, Y., Jayachandrababu, K.C., Hungerford, J.T., Dutzer, M.R., Ma, C., Walton, K.S., Sholl, D.S., et al. (2018). Acid gas stability of zeolitic imidazolate frameworks: generalized kinetic and thermodynamic characteristics. *Chem. Mater.* 30, 4089–4101.
23. Pang, S.H., Han, C., Sholl, D.S., Jones, C.W., and Lively, R.P. (2016). Facet-specific stability of ZIF-8 in the presence of acid gases dissolved in aqueous solutions. *Chem. Mater.* 28, 6960–6967.
24. Han, C., Zhang, C., Tymn<sup>nska</sup>, N., Schmidt, J.R., and Sholl, D.S. (2018). Insights into the stability of zeolitic imidazolate frameworks in humid acidic environments from first-principles calculations. *J. Phys. Chem. C* 122, 4339–4348.
25. Bennett, T.D., Cheetham, A.K., Fuchs, A.H., and Coudert, F.X. (2016). Interplay between defects, disorder and flexibility in metalorganic frameworks. *Nat. Chem.* 9, 11–16.
26. Liang, K., Coghlan, C.J., Bell, S.G., Doonan, C., and Falcaro, P. (2016). Enzyme encapsulation in zeolitic imidazolate frameworks: a comparison between controlled co-precipitation and biomimetic mineralisation. *Chem. Commun.* 52, 473–476.
27. Li, S., Dharmawardana, M., Welch, R.P., Benjamin, C.E., Shamir, A.M., Nielsen, S.O., and Gassensmith, J.J. (2018). Investigation of controlled growth of metal–organic frameworks on anisotropic virus particles. *ACS Appl. Mater. Interfaces* 10, 18161–18169.
28. Riccò, R., Liang, W., Li, S., Gassensmith, J.J., Caruso, F., Doonan, C., and Falcaro, P. (2018). Metal–organic frameworks for cell and virus biology: a perspective. *ACS Nano* 12, 13–23.
29. Liang, K., Ricco, R., Doherty, C.M., Styles, M.J., and Falcaro, P. (2016). Amino acids as biomimetic crystallization agents for the synthesis of ZIF-8 particles. *CrystEngComm* 18, 4264–4267.
30. Low, Z.-X., Yao, J., Liu, Q., He, M., Wang, Z., Suresh, A.K., Bellare, J., and Wang, H. (2014). Crystal transformation in zeolitic-imidazolate framework. *Cryst. Growth Des.* 14, 6589–6598.
31. Jiang, J.Q., Yang, C.X., and Yan, X.P. (2013). Zeolitic imidazolate framework-8 for fast adsorption and removal of benzotriazoles from aqueous solution. *ACS Appl. Mater. Interfaces* 5, 9837–9842.
32. Ryder, M.R., Civalleri, B., Bennett, T.D., Henke, S., Rudi<sup>c</sup>, S., Cinque, G., Fernandez-Alonso, F., and Tan, J.C. (2014). Identifying the role of terahertz vibrations in metal–organic frameworks: from gate-opening phenomenon to shear-driven structural destabilization. *Phys. Rev. Lett.* 113, 215502.
33. Kumari, G., Jayaramulu, K., Maji, T.K., and Narayana, C. (2013). Temperature induced structural transformations and gas adsorption in the zeolitic imidazolate framework ZIF-8: a Raman study. *J. Phys. Chem. A* 117, 11006–11012.
34. Socrates, G. (2010). *Infrared and Raman Characteristic Group Frequencies: Tables and Charts*, Third Edition (Wiley).
35. Hermans, J.J., Keune, K., van Loon, A., and Iedema, P.D. (2015). An infrared spectroscopic study of the nature of zinc carboxylates in oil paintings. *J. Anal. At. Spectrom.* 30, 1600–1608.
36. Chen, R., Yao, J., Gu, Q., Smeets, S., Baerlocher, C., Gu, H., Zhu, D., Morris, W., Yaghi, O.M., and Wang, H. (2013). A twodimensional zeolitic imidazolate framework with a cushion-shaped cavity for CO<sub>2</sub> adsorption. *Chem. Commun.* 49, 9500–9502.
37. Li, X., Li, Z., Lu, L., Huang, L., Xiang, L., Shen, J., Liu, S., and Xiao, D.R. (2017). The solvent induced inter-dimensional phase transformations of cobalt zeolitic-imidazolate frameworks. *Chem. Eur. J.* 23, 10638–10643.
38. Huang, X.C., Lin, Y.Y., Zhang, J.P., and Chen, X.M. (2006). Ligand-directed strategy for zeolite-type metal–organic frameworks: zinc(II) imidazolates with unusual zeolitic topologies. *Angew. Chem. Int. Ed.* 45, 1557–1559.
39. Shen, K., Zhang, L., Chen, X., Liu, L., Zhang, D., Han, Y., Chen, J., Long, J., Luque, R., Li, Y., et al. (2018). Ordered macro-microporous metalorganic framework single crystals. *Science* 359, 206–210.
40. Pregosin, P.S. (2008). <sup>31</sup>P and <sup>13</sup>C NMR studies on metal complexes of phosphorus-donors: recognizing surprises. *Coord. Chem. Rev.* 252, 2156–2170.
41. Cheng, G., Li, W., Ha, L., Han, X., Hao, S., Wan, Y., Wang, Z., Dong, F., Zou, X., Mao, Y., et al. (2018). Self-assembly of extracellular vesicle-like metal–organic framework nanoparticles for protection and intracellular delivery of biofunctional proteins. *J. Am. Chem. Soc.* 140, 7282–7291.
42. Maddigan, N.K., Tarzia, A., Huang, D.M., Sumbly, C.J., Bell, S.G., Falcaro, P., and Doonan, C.J. (2018). Protein surface functionalisation as a general strategy for facilitating biomimetic mineralisation of ZIF-8. *Chem. Sci.* 9, 4217–4223.
43. Liang, W., Ricco, R., Maddigan, N.K., Dickinson, R.P., Xu, H., Li, Q., Sumbly, C.J., Bell, S.G., Falcaro, P., and Doonan, C.J. (2018). Control of structure topology and spatial distribution of biomacromolecules in protein@ZIF-8 biocomposites. *Chem. Mater.* 30, 1069–1077.
44. Gitlin, I., Carbeck, J.D., and Whitesides, G.M. (2006). Why are proteins charged? networks of charge–charge interactions in proteins measured by charge ladders and capillary electrophoresis. *Angew. Chem. Int. Ed.* 45, 3022–3060.
45. Hess, B., and van der Vegt, N.F.A. (2009). Cation specific binding with protein surface charges. *Proc. Natl. Acad. Sci. USA* 106, 13296–13300.
46. Cui, J., Feng, Y., Lin, T., Tan, Z., Zhong, C., and Jia, S. (2017). Mesoporous metal–organic framework with well-defined cruciate flower-like morphology for enzyme immobilization. *ACS Appl. Mater. Interfaces* 9, 10587–10594.
47. Liang, W., Xu, H., Carraro, F., Maddigan, N.K., Li, Q., Bell, S.G., Huang, D.M., Tarzia, A., Solomon, M.B., Amenitsch, H., et al. (2019). Enhanced activity of enzymes encapsulated in hydrophilic metal–organic frameworks. *J. Am. Chem. Soc.* 141, 2348–2355.
48. Burtch, N.C., Jasuja, H., and Walton, K.S. (2014). Water stability and adsorption in metal–organic frameworks. *Chem. Rev.* 114, 10575–10612.
49. McHugh, L.N., McPherson, M.J., McCormick, L.J., Morris, S.A., Wheatley, P.S., Teat, S.J., McKay, D., Dawson, D.M., Sansome, C.E.F., Ashbrook, S.E., et al. (2018). Hydrolytic stability in hemilabile metal–organic frameworks. *Nat. Chem.* 10, 1096–1102.
50. Wang, T., Farajollahi, M., Henke, S., Zhu, T., Bajpe, S.R., Sun, S., Barnard, J.S., Lee, J.S., Madden, J.D.W., Cheetham, A.K., et al. (2017). Functional conductive nanomaterials via polymerisation in nano-channels: PEDOT in a MOF. *Mater. Horiz.* 4, 64–71.
51. Uemura, T., Yanai, N., and Kitagawa, S. (2009). Polymerization reactions in porous coordination polymers. *Chem. Soc. Rev.* 38, 1228–1236.

## Supplemental Scheme Section



Scheme S1. Schematic diagram of the direct visual approach for catalase activity.

## Supplemental Figure Section

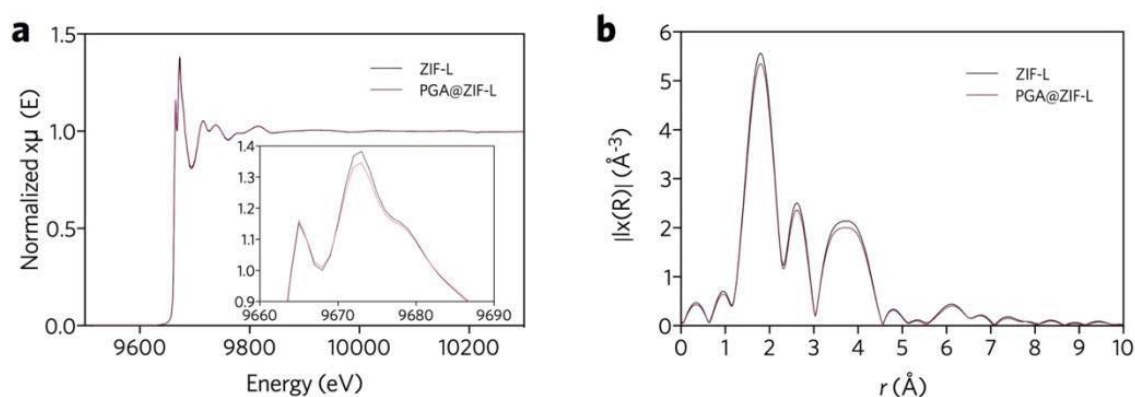


Figure S1. XAFS characterization of the PGA@ZIF-L and pure ZIF-L. (a) XANES spectra at the Zn K-edge. (b) Fourier transformed (FT) EXAFS spectra.

We applied XAFS technique to study the structure variance for the composite at an atomic scale. The Zn K-edge XANES spectrum displayed a pre-edge peak around 9655 eV and a strong peak around 9670 eV (Figure S1a). Without shifts in the peak position, the intensity reduction in the main peak (9670 eV), which normally refers to the interference from single-scattering of the neighboring scattering center, is directly linked to the reduced valency of the Zn ions. The EXAFS observation (Figure S1b) suggests a loss of ligands in the first coordination shell around Zn, possibly due to the steric hindrance by the bulkier PGA chains bonded to Zn ions.<sup>1</sup> It should be noted that due to overlapping Zn-N and Zn-O bond lengths, it is difficult to differentiate the Zn-O bond between Zn and PGA, and the Zn-N imidazole bond in the EXAFS results, hence other measurement techniques were required.

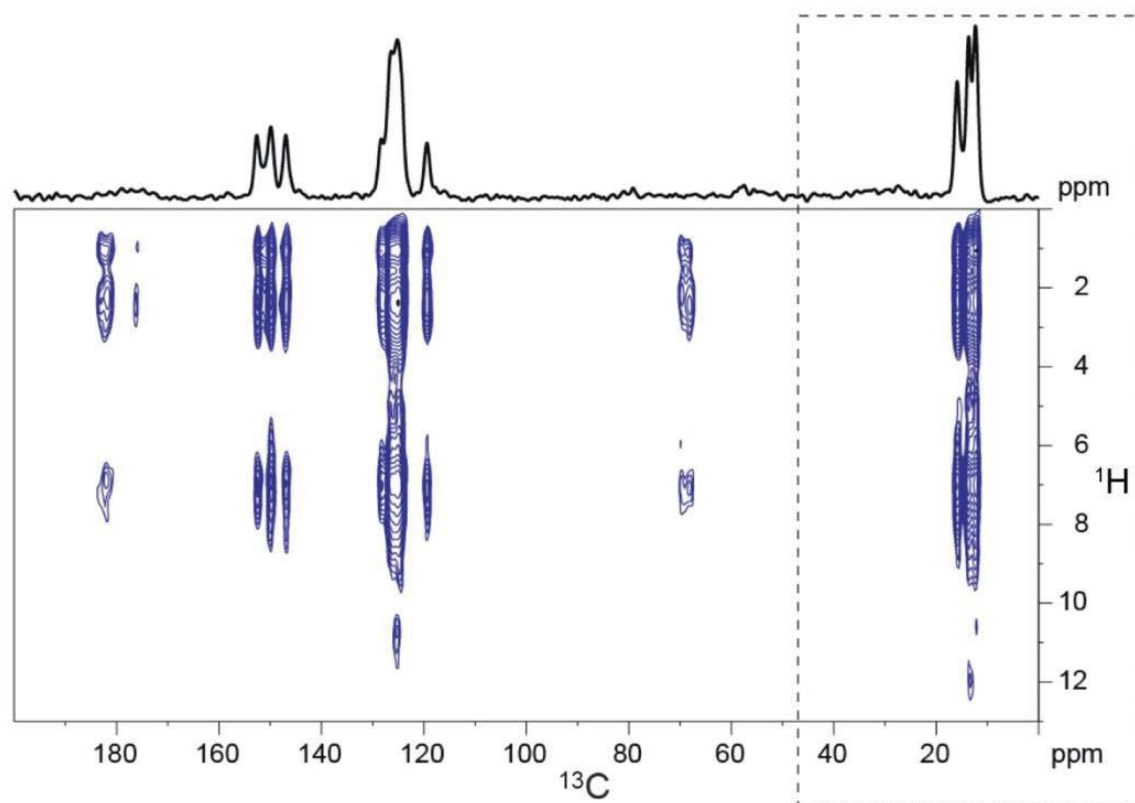


Figure S2. **2D  $^{13}\text{C}\{^1\text{H}\}$  HETCOR for the PGA@ZIF-L system.** The spectra are acquired after 10 ms of  $^1\text{H}$  spin diffusion. Figure. S2 is the full spectrum, while the spectral region of the methyl  $^{13}\text{C}$  peaks indicated by the dashed square expanded in Figure 2b in the main text.

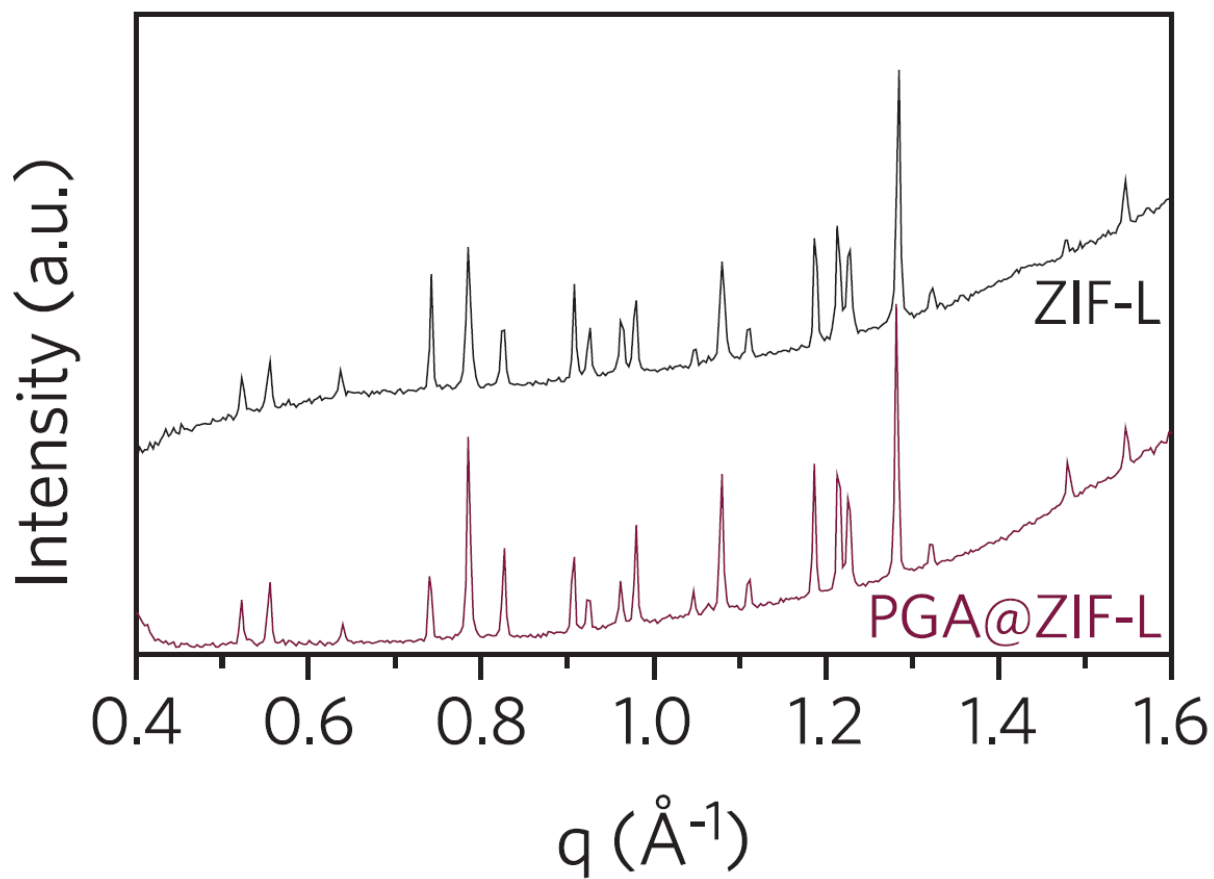


Figure S3. Synchrotron SAXS patterns of PGA@ZIF-L (red) and reference ZIF-L crystals (black).

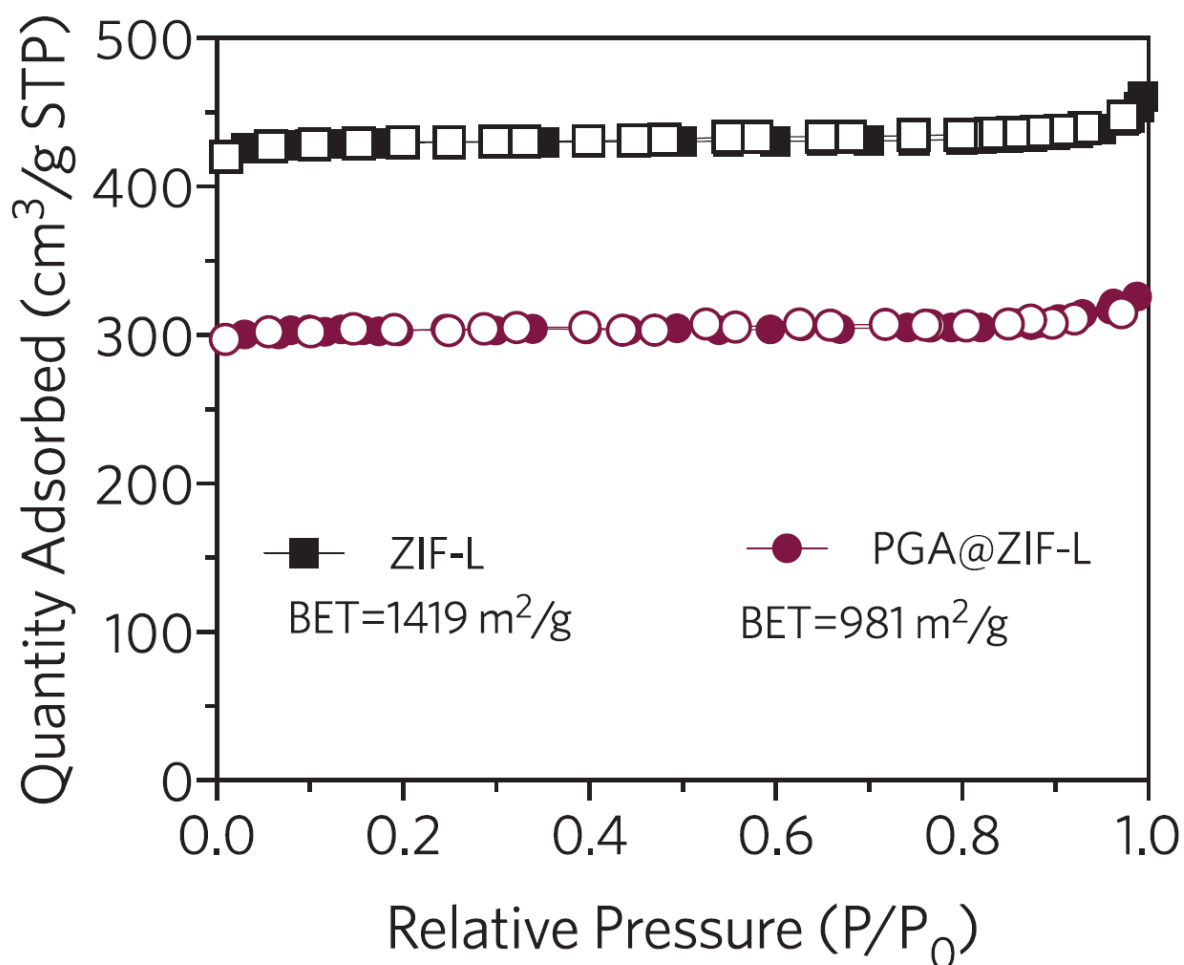


Figure S4. N<sub>2</sub> isothermal at 77K of PGA@ZIF-L (red) and reference ZIF-L crystals (black).

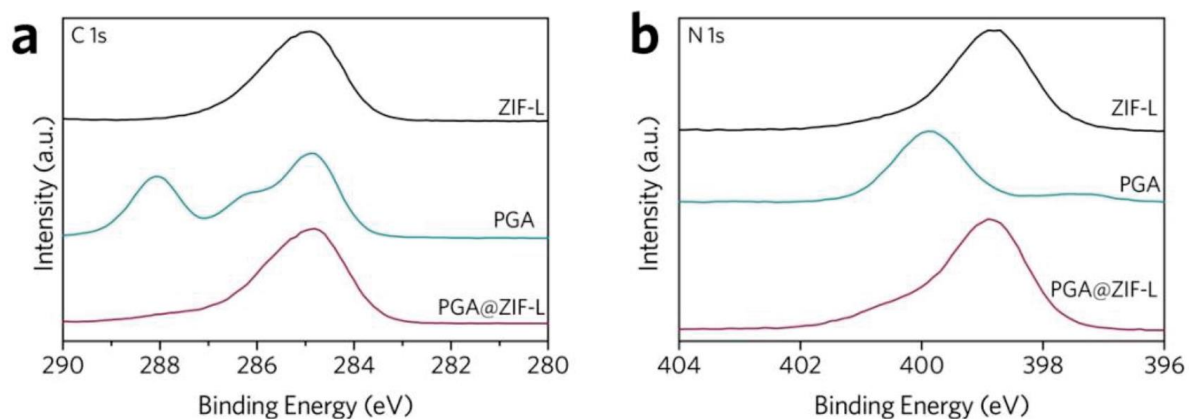


Figure S5. XPS (a) C 1s and (b) N 1s spectra of the PGA@ZIF-L (red), PGA (green) and ZIF-L (black).

The main peak for the C 1s spectra correlates to the C-C bond electron environment at 284.8 eV. The shoulder peak of N 1s at around 400.5 eV for PGA@ZIF-L can be attributed to the presence of PGA in the composite. However, no clear peak shift was observed in the C 1s and N 1s spectra when compare the pure phase against the composite, suggesting the interactions on C and N atoms are relatively weak.

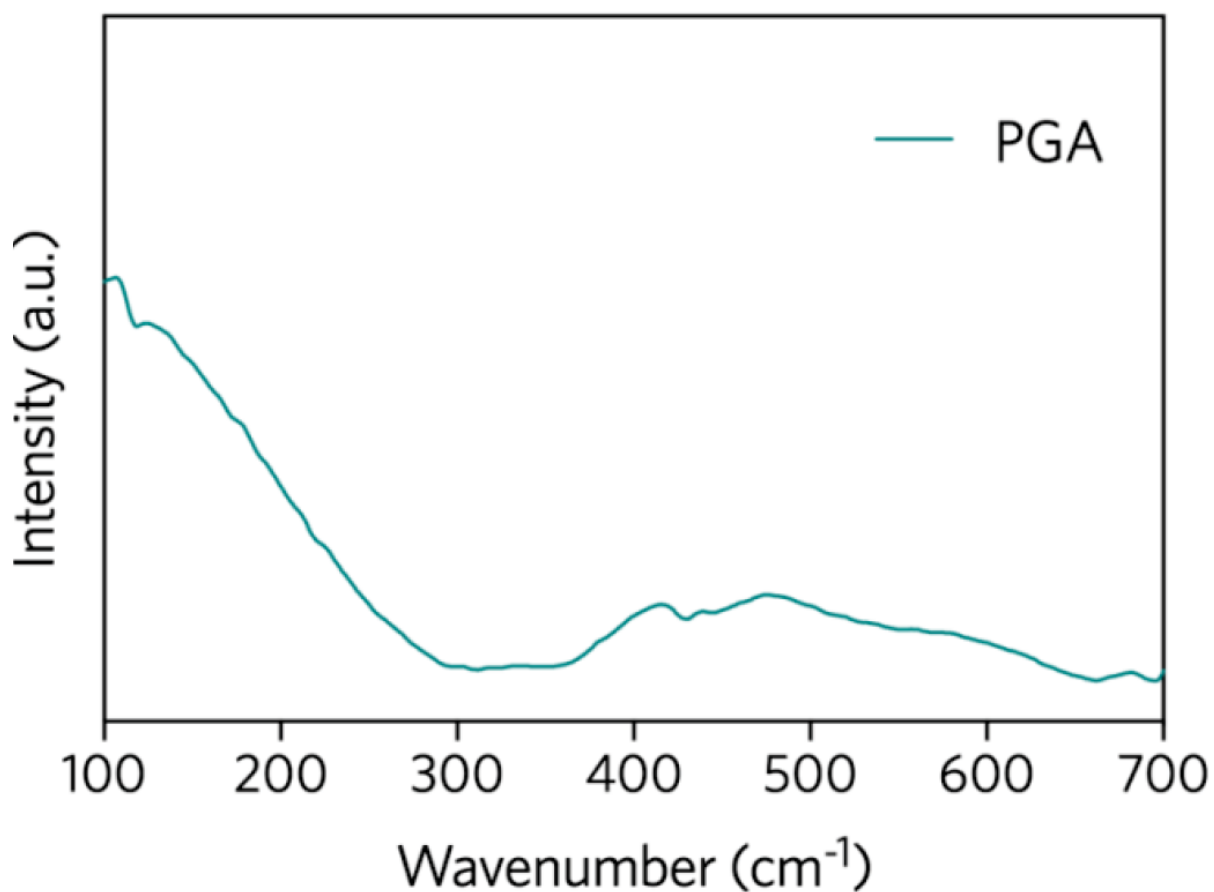


Figure S6. THz-FIR radiation of PGA polypeptide, showing no distinct feature in the tested wavenumber range.

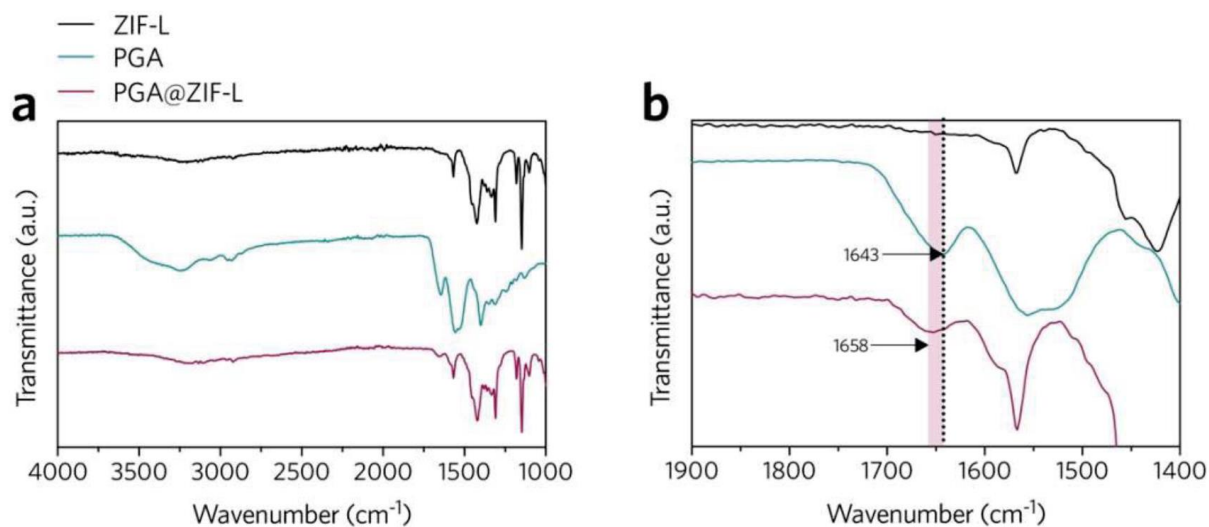


Figure S7. FTIR spectra of PGA@ZIF-L (red), PGA (green) and ZIF-L (black), with highlighted carboxyl peak shift in panel (b).

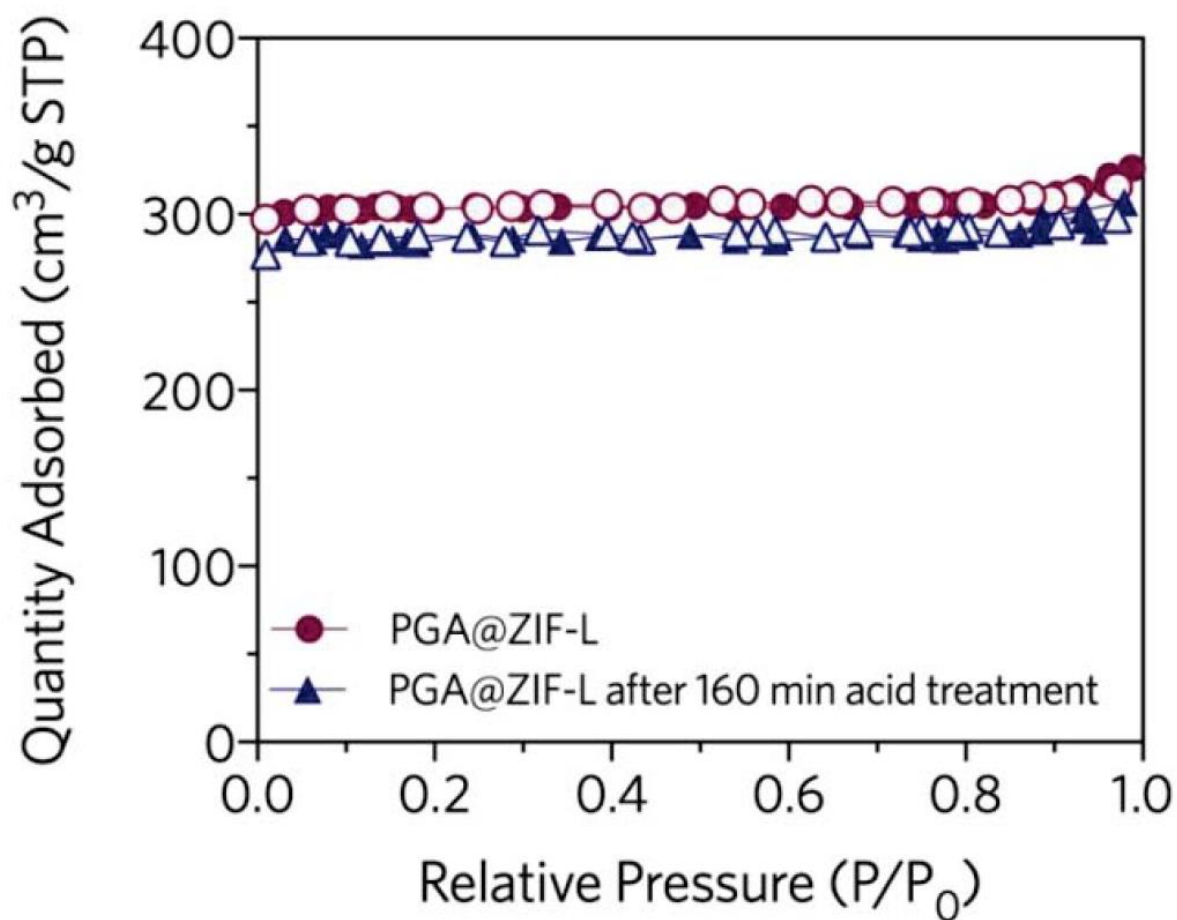


Figure S8. Gas adsorption for the PGA@ZIF-L before and after the acid treatment.

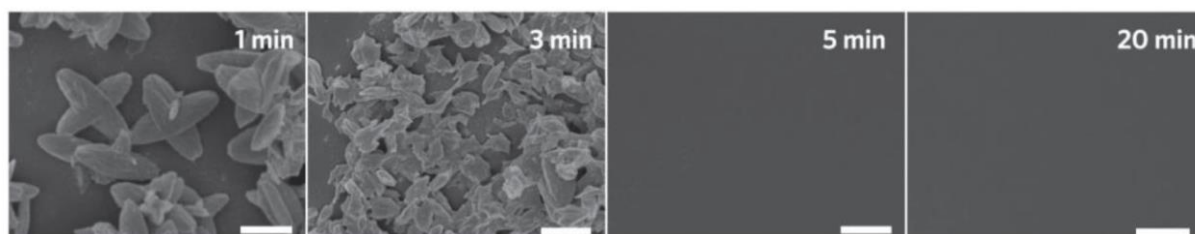


Figure S9. SEM image of the pure ZIF-L with different incubation time in 50 mM acetate buffer. Scale bars are 2 $\mu$ m.

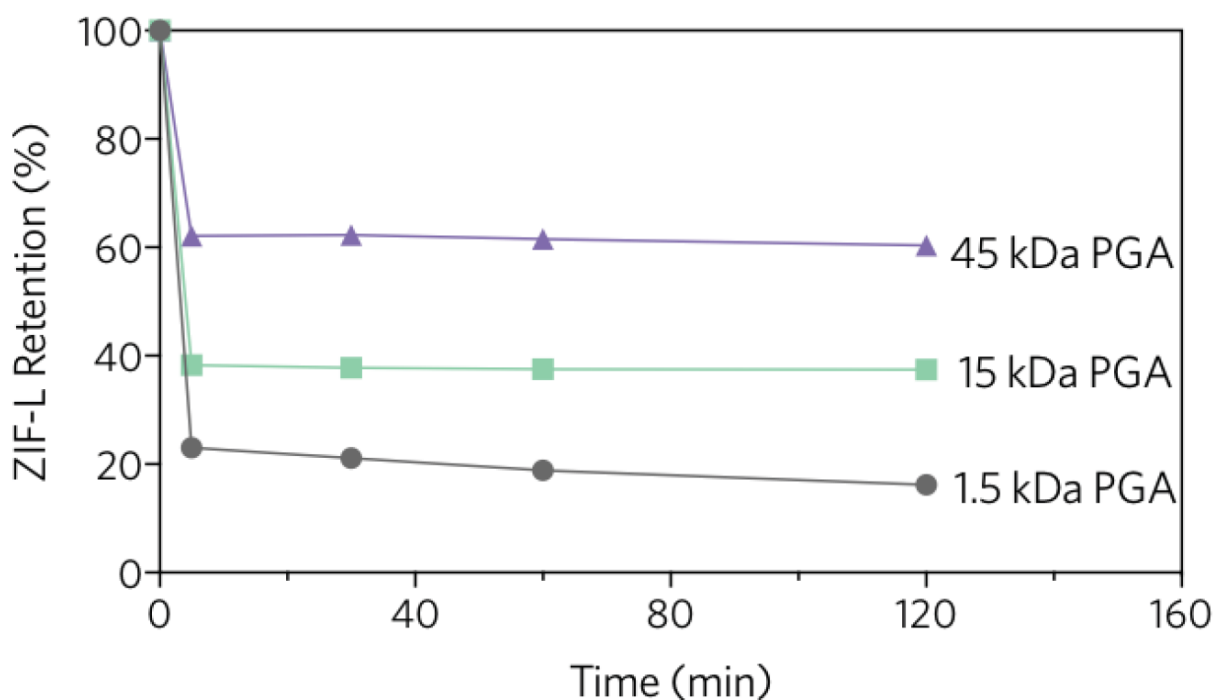


Figure S10. **Effect of PGA molecular weight on the PGA@ZIF-L acid stability.** 0.22  $\mu\text{mol}$  of PGA was applied for the synthesis. The results are based on the dissolved Zn ion concentration in the supernatant monitored by ICP-MS when exposing the composite to pH 5 acetate buffer. The encapsulation efficiency for all PGA were higher than 98%.

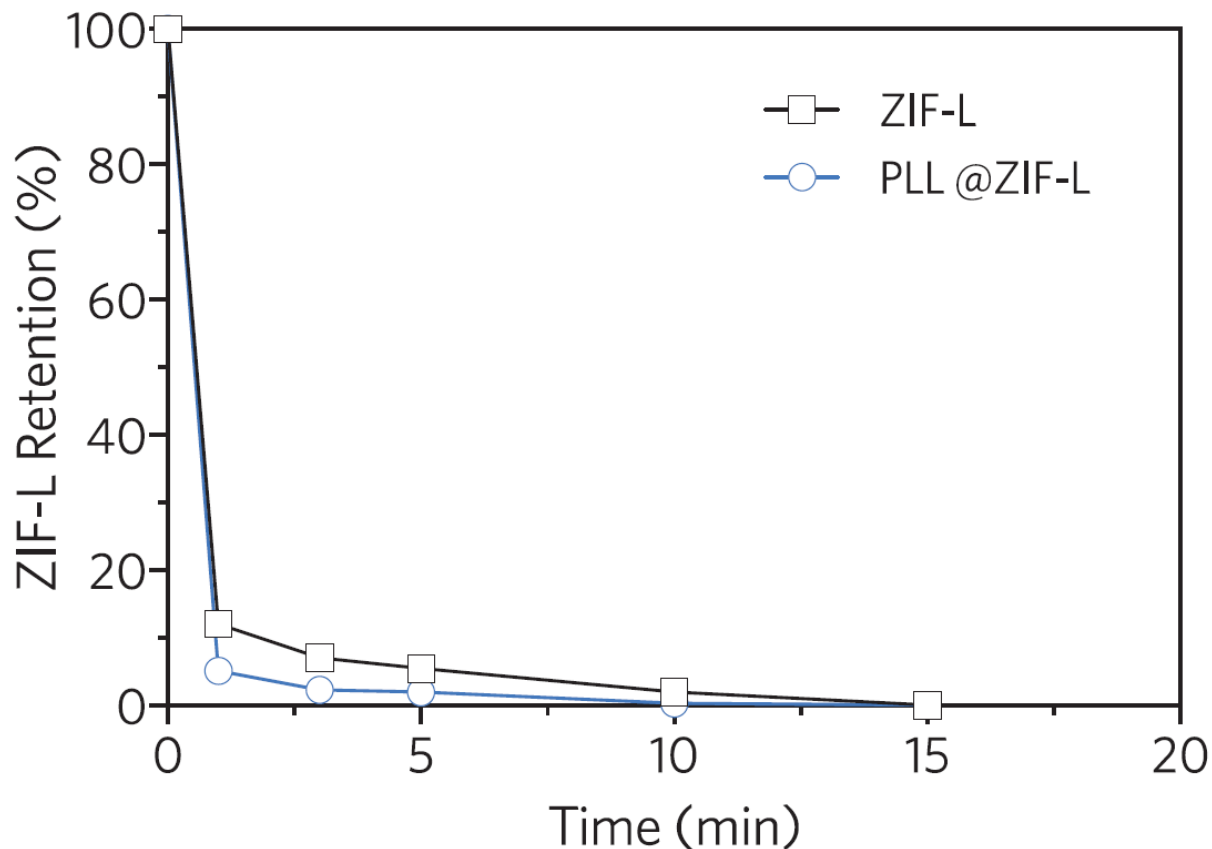


Figure S11. **ZIF-L retention for PLL@ZIF-L and ZIF-L during the acid treatment process in acetate acid.** The results are based on the dissolved Zn ion concentration in the supernatant monitored by ICP-MS.

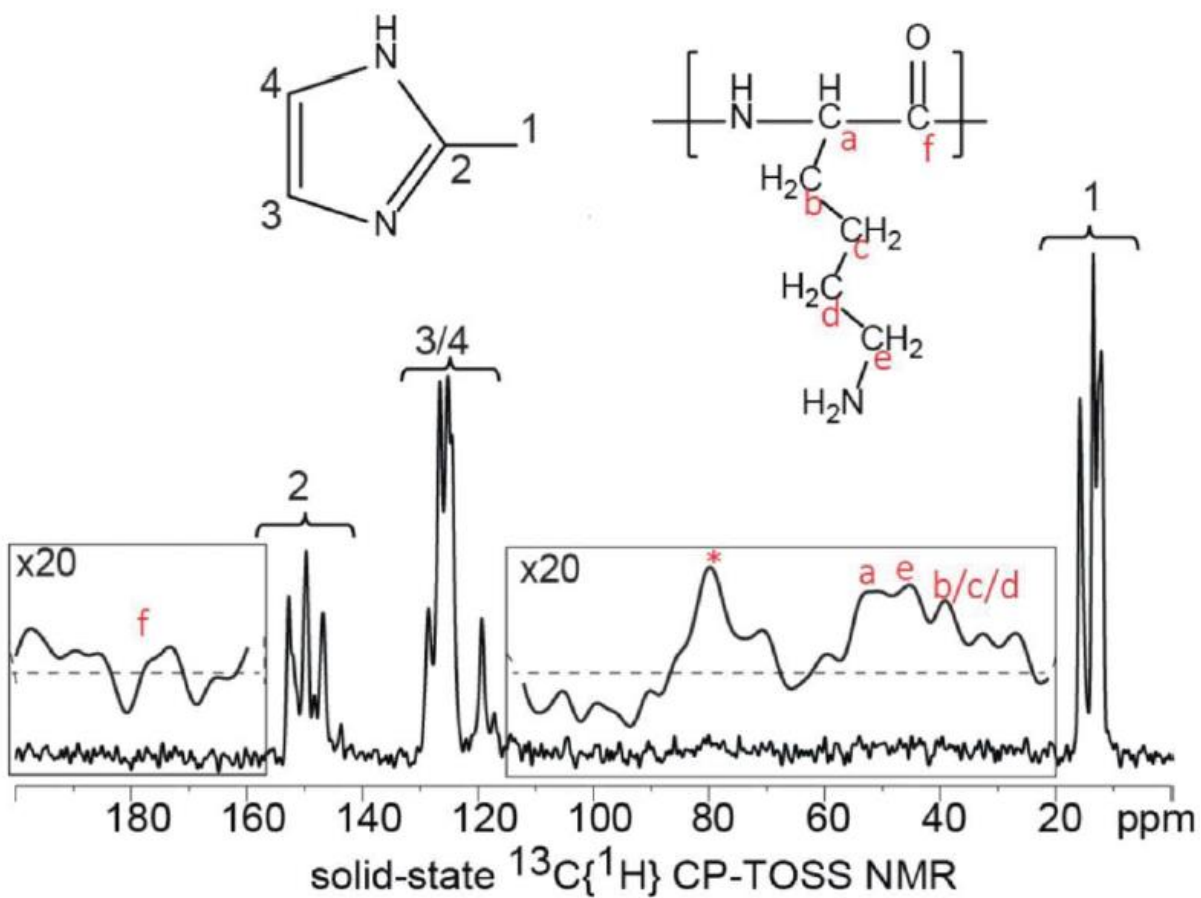


Figure S12. 1D  $^{13}\text{C}$  NMR results of the PLL@ZIF-L, along with peak assignments.

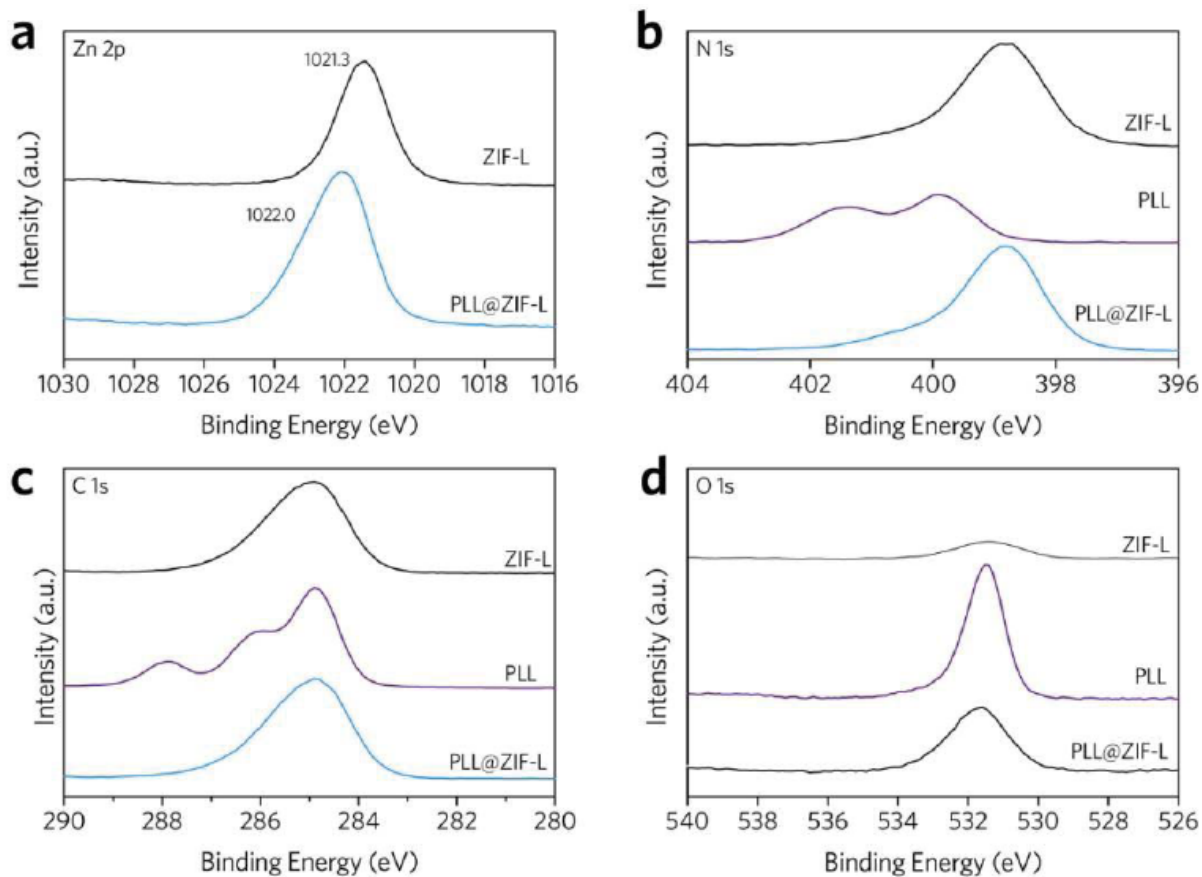


Figure S13. XPS (a) Zn 2p, (b) N 1s, (c) C 1s, and (d) O 1s spectra of the PLL@ZIF-L, pure PLL and pure ZIF-L.

A clear peak shift was observed in the Zn 2p spectrum for PLL@ZIF-L compared with pure ZIF-L, indicating the change of electron distribution for the Zn atoms. In this system, the most probable emerging coordination bond would be between the primary amine and Zn nodes. However, the peak position change from N 1s was less obvious, possibly due to the presence of a large amount of N atoms with different coordination environments on both the framework and the polypeptide. The presence of O1s peak for pure ZIF-L is originated from the surface uncoordinated Zn nodes, where water can be absorbed.

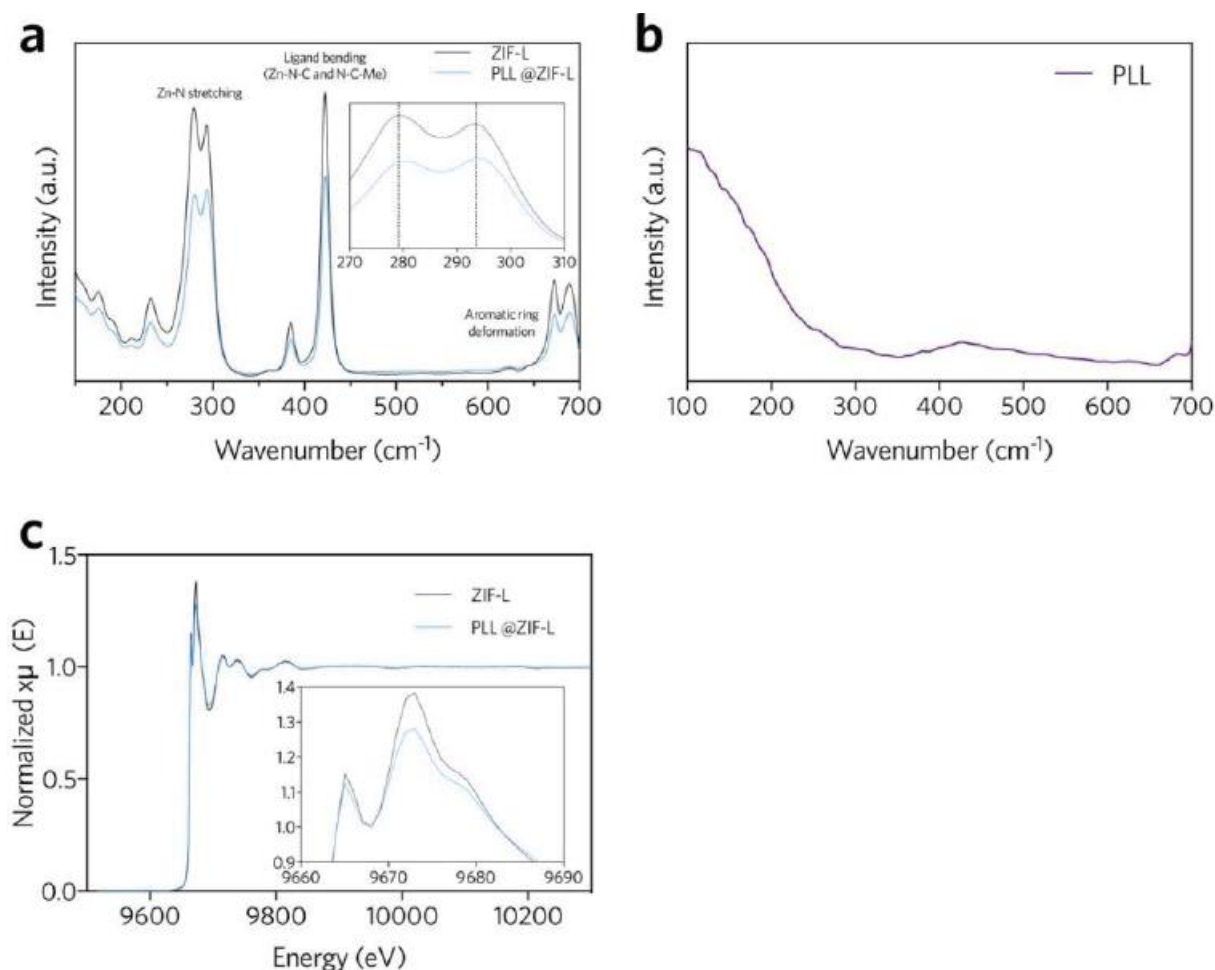


Figure S14. **Synchrotron THz FIR and XAFS characterization of the PGA@ZIF-L and pure ZIF-L.** (a) THz FIR pattern of the ZIF-L and PLL@ZIF-L, with the insert showing negligible peak shift for the Zn-N stretching bond. (b) THz FIR pattern of the pure PLL benchmark, showing no distinct feature in the THz region. (c) Zn K-edge X-ray absorption near edge structure spectra.

The XPS and XANES spectra both indicate the emergence of a new bond between Zn and N on the amine group. However, this has a negligible effect on the Zn-N bonding strength for ZIF-L (THz FIR, Figure S14ab), and subsequently has no contribution to the acidic stability for the PLL@ZIF-L composite. During the dissolution process, acid acts as a catalyst, and the acid stability of ZIFs is ruled by the thermodynamic and kinetic parameters. The incorporation of bulkier polypeptide molecules could increase the mass transfer resistance for water/acid molecules to approach the Zn-N bond, and the hydrophilic region on the polypeptide can bond with water molecules, suppressing its attack to the Zn nodes.<sup>2</sup> However, considering the similar main chain structure for PGA and PLL, these aspects are not the major contributing factor towards the improved stability. Therefore, the newly formed Zn-O bond for PGA@ZIF-L can increase the strength for Zn-N bond, and the carboxylate group connected to the Zn center increases the steric hindrance for the Zn tetrahedron to re-organize during the dissolution process, leading to a higher stability.

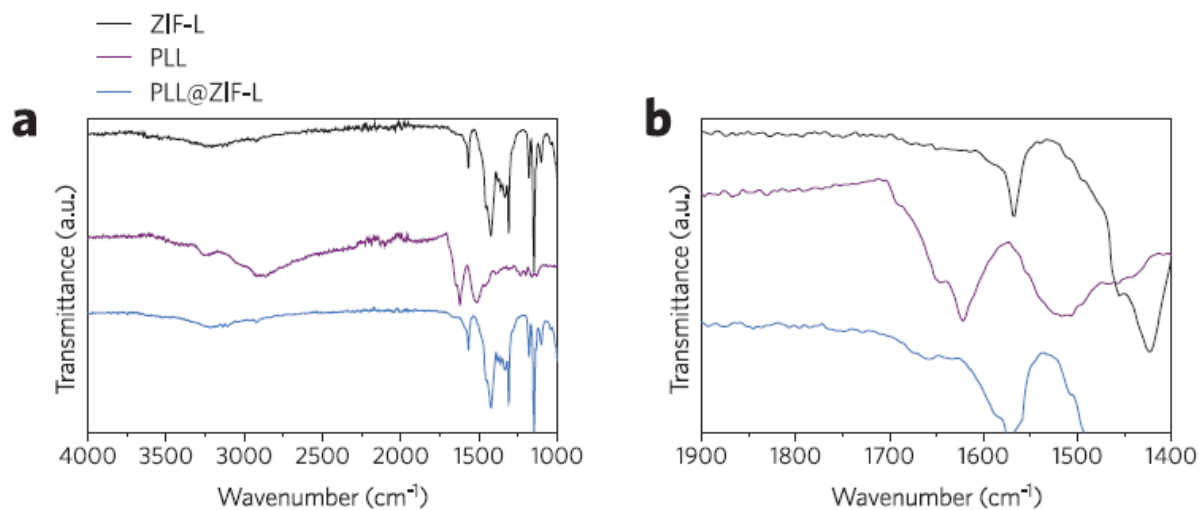


Figure S15. FTIR spectra of PLL@ZIF-L (blue), PGA (purple) and ZIF-L (black), with highlighted amine peak region in panel (b).

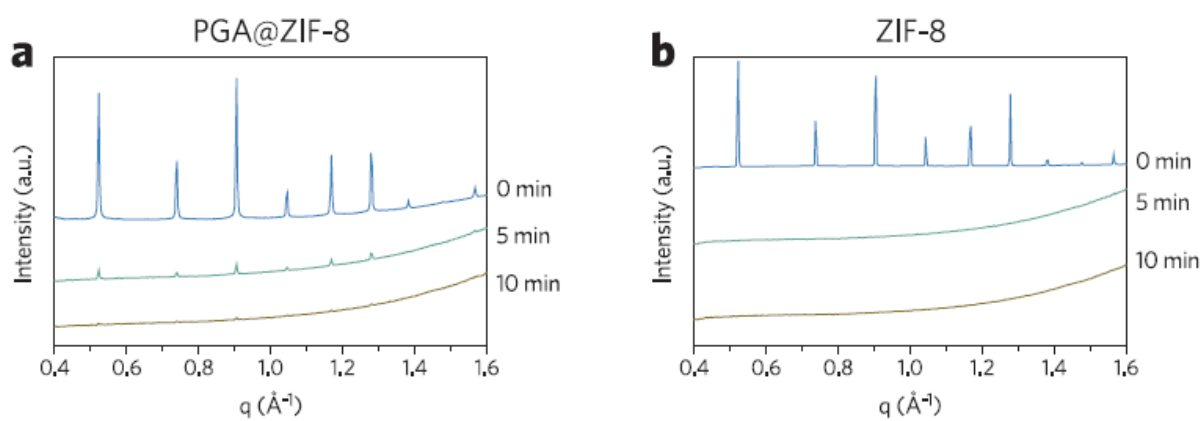


Figure S16. *Ex-situ* SAXS pattern variance during the dissolution process for PGA@ZIF-8 and pure ZIF-8.

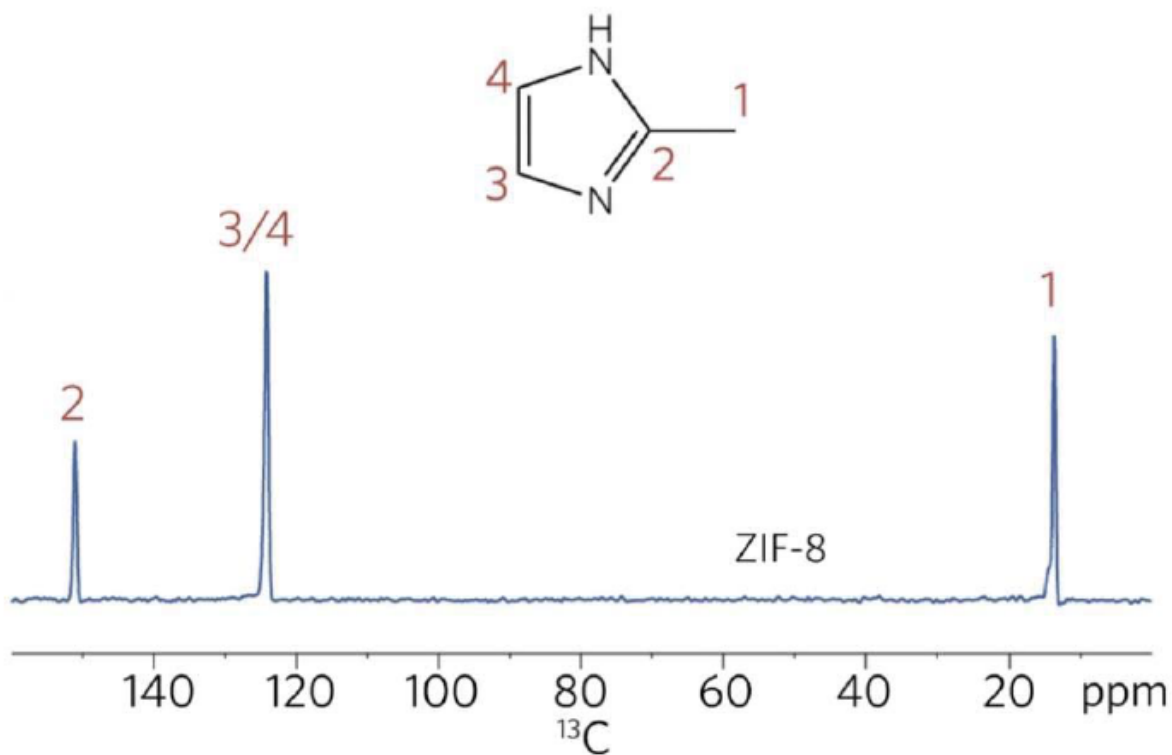


Figure S17.  $^{13}\text{C}$  NMR spectrum of ZIF-8, along with peak assignments.

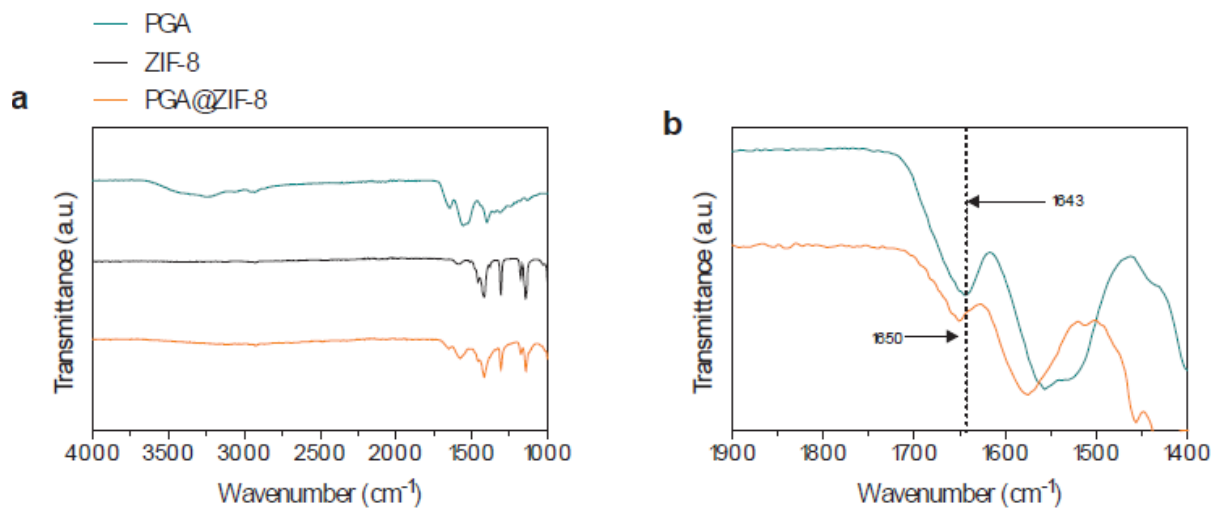


Figure S18. FTIR spectra of PGA@ZIF-8 (orange), PGA (green) and ZIF-8 (black), with highlighted carboxyl peak shift in panel (b).

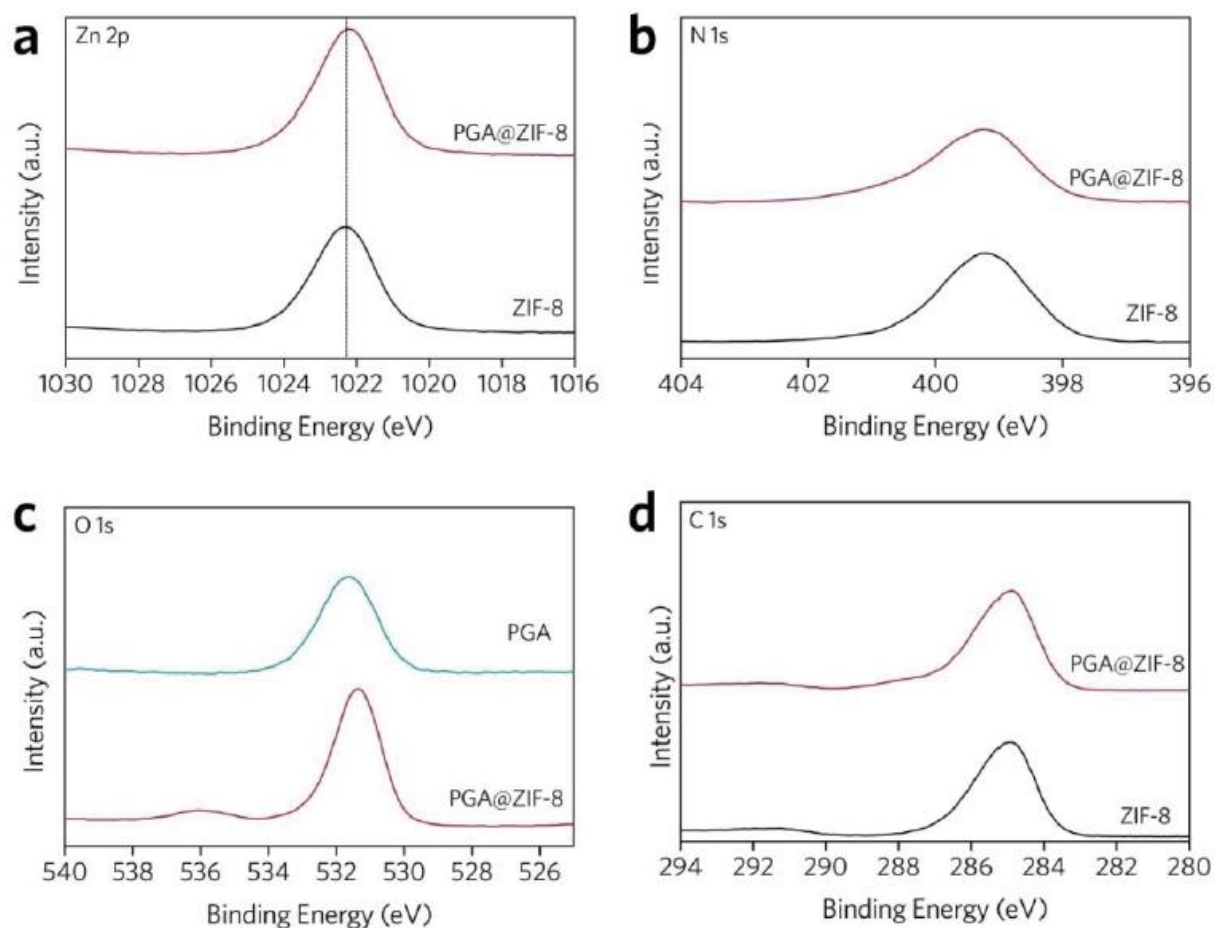


Figure S19. XPS (a) Zn 2p, (b) N1s, (c) O1s, and (d) C 1s spectra of the PGA@ZIF-8 and pure ZIF-8.

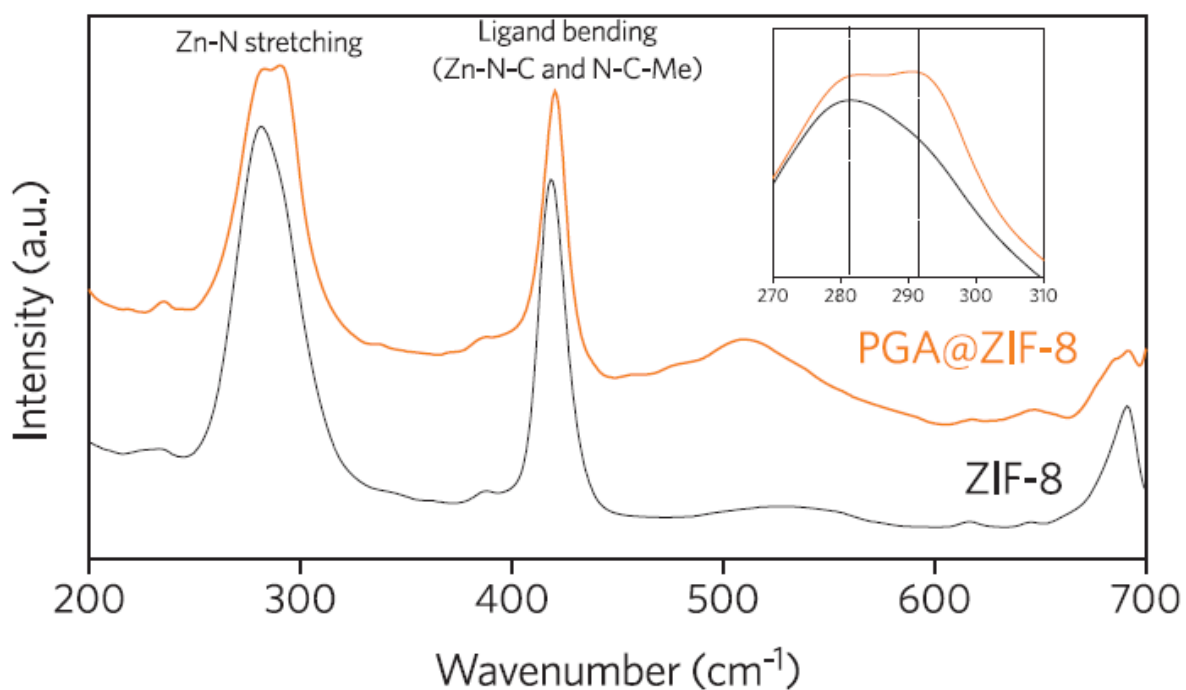


Figure S20. Synchrotron THz FIR of the PGA@ZIF-8 and pure ZIF-8.

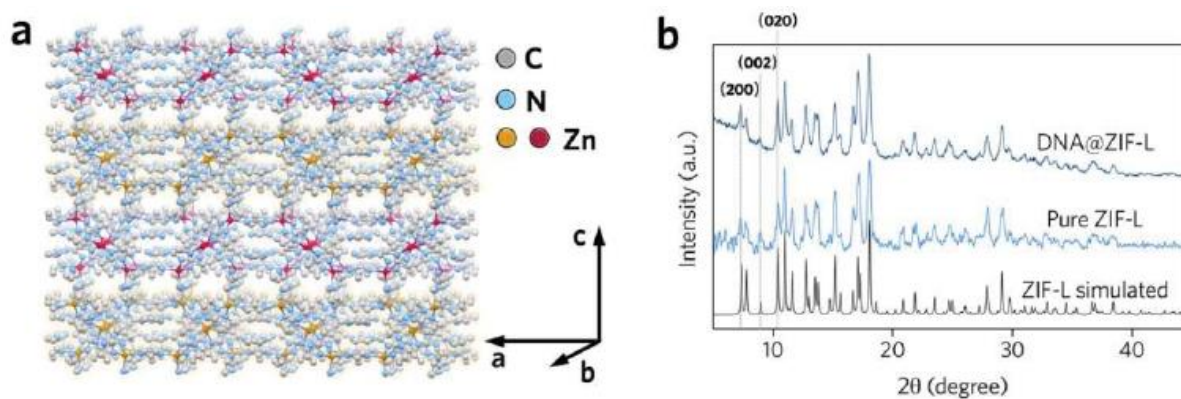


Figure S21. **Structural properties of DNA@ZIF-L.** (a) Schematic diagram of the ZIF-L crystal structure, with the neighbouring nanosheet highlighted with different coloured Zn atoms. (b) XRD patterns of the simulated ZIF-L, pure ZIF-L powder and DNA@ZIF-L composite.

Based on the XRD results, the signature peaks correlating to the (200), (020) and (002) crystal planes were preserved for DNA@ZIF-L. Further, Pawley refinement results (Table S3) confirm the ZIF-L crystal structure is largely invariant after incorporating DNA within the framework. The unchanged ZIF-L crystal structure suggests the DNA molecules are not simply sandwiched between the 2D layered nanosheets within the intergallery channels.

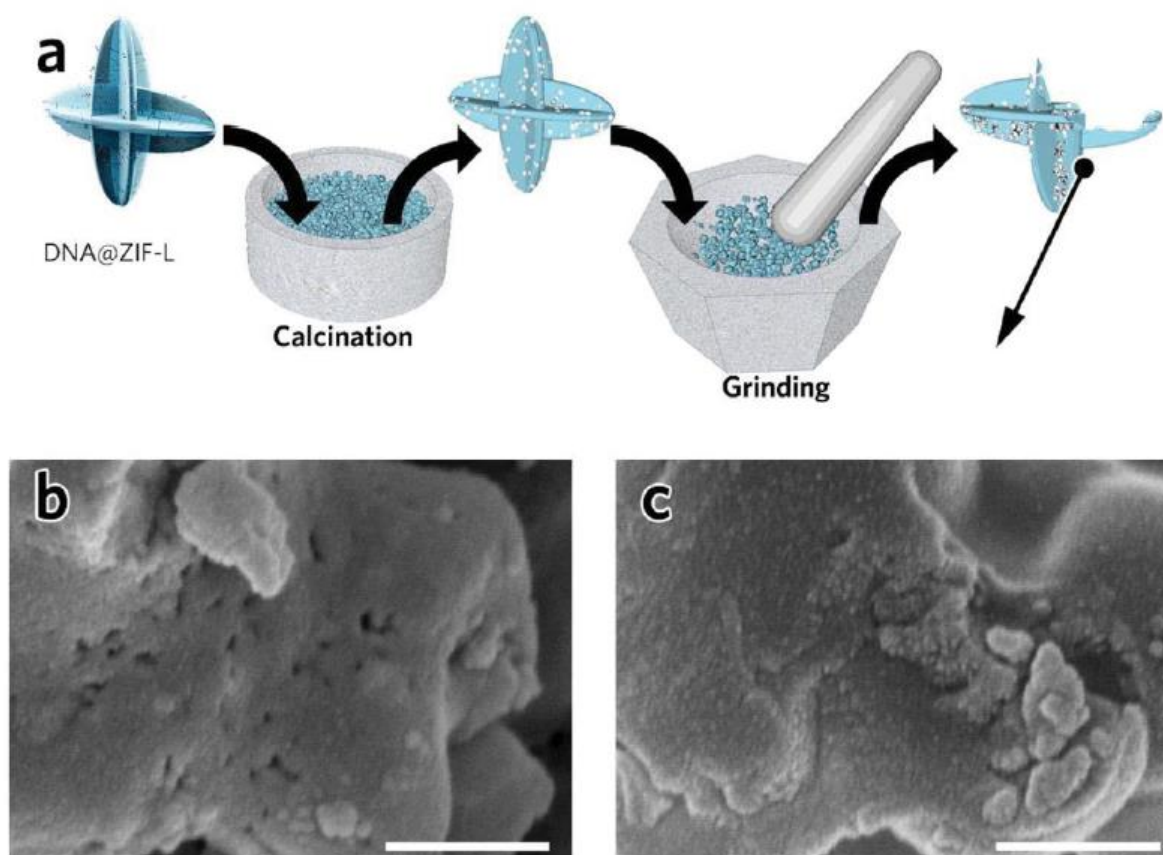


Figure S22. **DNA@ZIF-L calcination and cross-sectional SEM image.** (a) Schematic diagram of the DNA@ZIF-L calcination and grinding process to obtain the cross-sectional region. Cross-sectional SEM images of (b) DNA@ZIF-L and (c) pure ZIF-L subject to the same treatment. Scale bars are 500 nm. DNA molecules can be removed from the composite by calcination treatment at 250 °C for 1 h in air, leaving a void structure where the DNA was originally located (Figure S22a). Then the distribution of such structure within the ZIF-L can provide information on the original DNA distribution within the

composite. As shown in Figure S22b, at the cross-sectional region of the calcinated DNA@ZIF-L, the voids were relatively even. At the same time, the presence of relatively large voids on the scale of 20-40 nm suggests the DNA is present in a folded form in the DNA@ZIF-L, rather than in their extended strand structure. At the same time, the pure ZIF-L shows no such void structure after the same calcination treatment (Figure S22c).

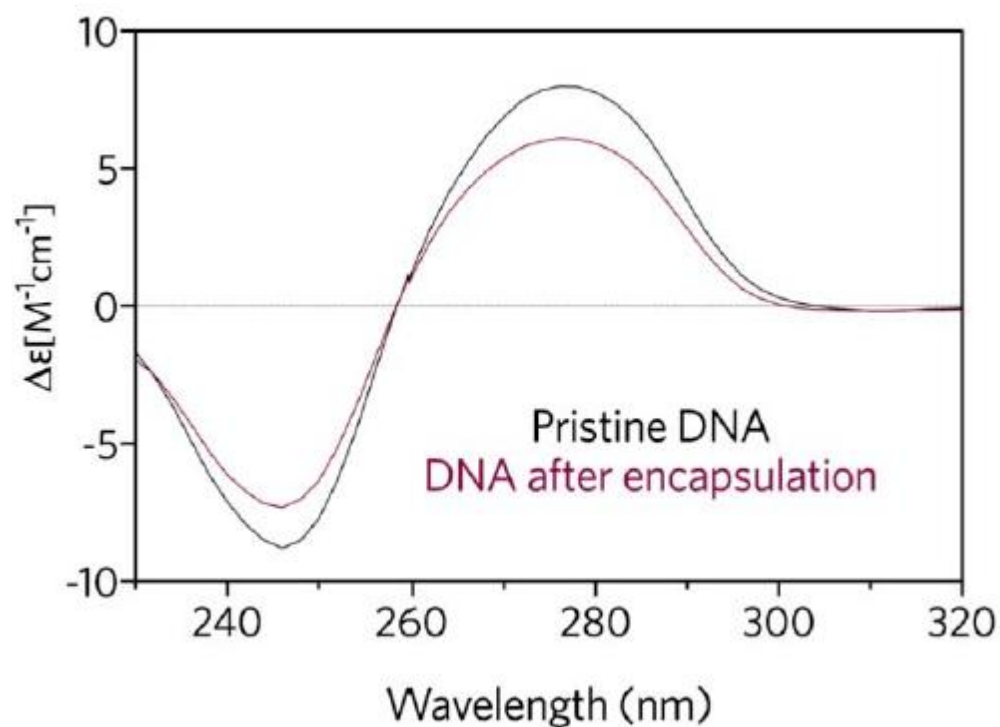


Figure S23. **Conformational study of DNA and DNA@ZIF-L by circular dichroism.**

Circular dichroism (CD) spectroscopy is very sensitive in determining the conformational properties of DNA. The DNA conformations before and after ZIF-L encapsulation were determined. Based on the CD results, the B-type double-helix structure of DNA was largely invariant, suggesting the ZIF encapsulation process is relatively benign.<sup>3-5</sup>

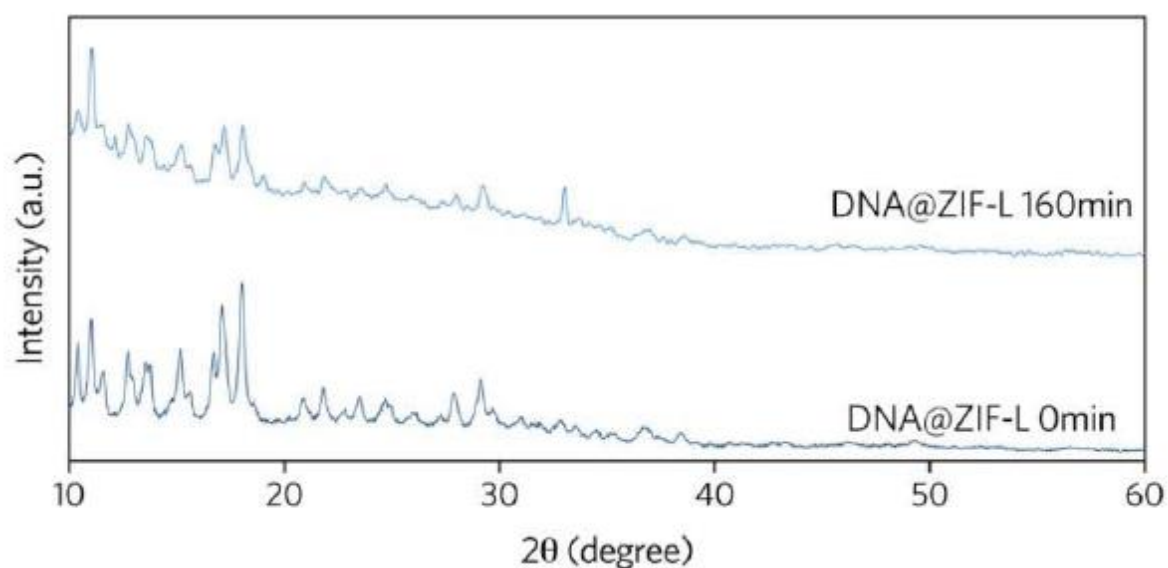


Figure S24. **Acidic stability of DNA@ZIF-L in the presence of pH 5 acetate acid.** XRD patterns of DNA@ZIF-L before and after acid treatment.

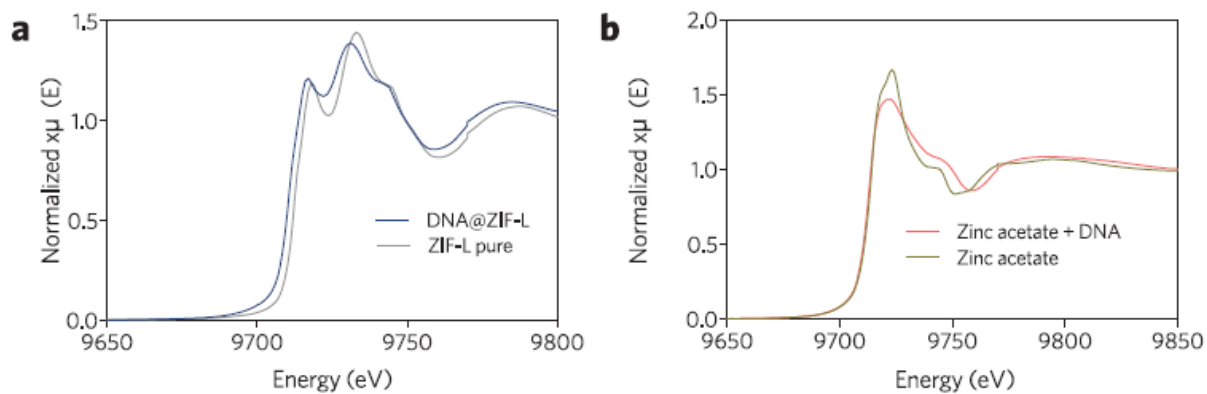


Figure S25. **XANES spectra for the characterization of the DNA@ZIF-L and zinc acetate/DNA solution.** (a) Zn K-edge XANES spectra for pure ZIF-L and DNA@ZIF-L. (b) Zn K-edge XANES spectra for zinc acetate solution and zinc acetate/DNA solution mixtures.

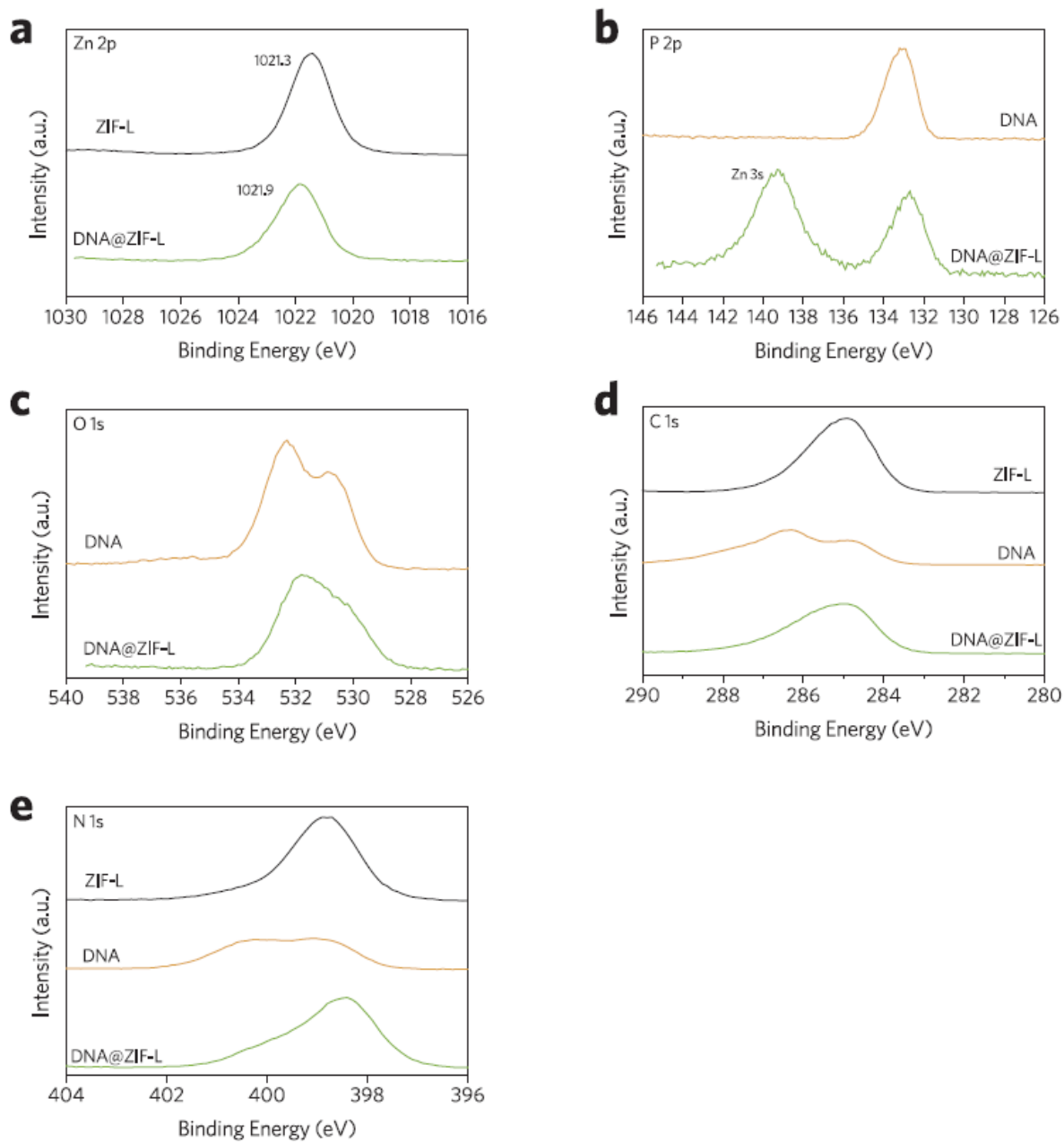


Figure S26. XPS (a) Zn 2p, (b) P 2p, (c) O 1s, (d) C 1s, and (e) N 1s spectra of the DNA@ZIF-L, DNA and pure ZIF-L.

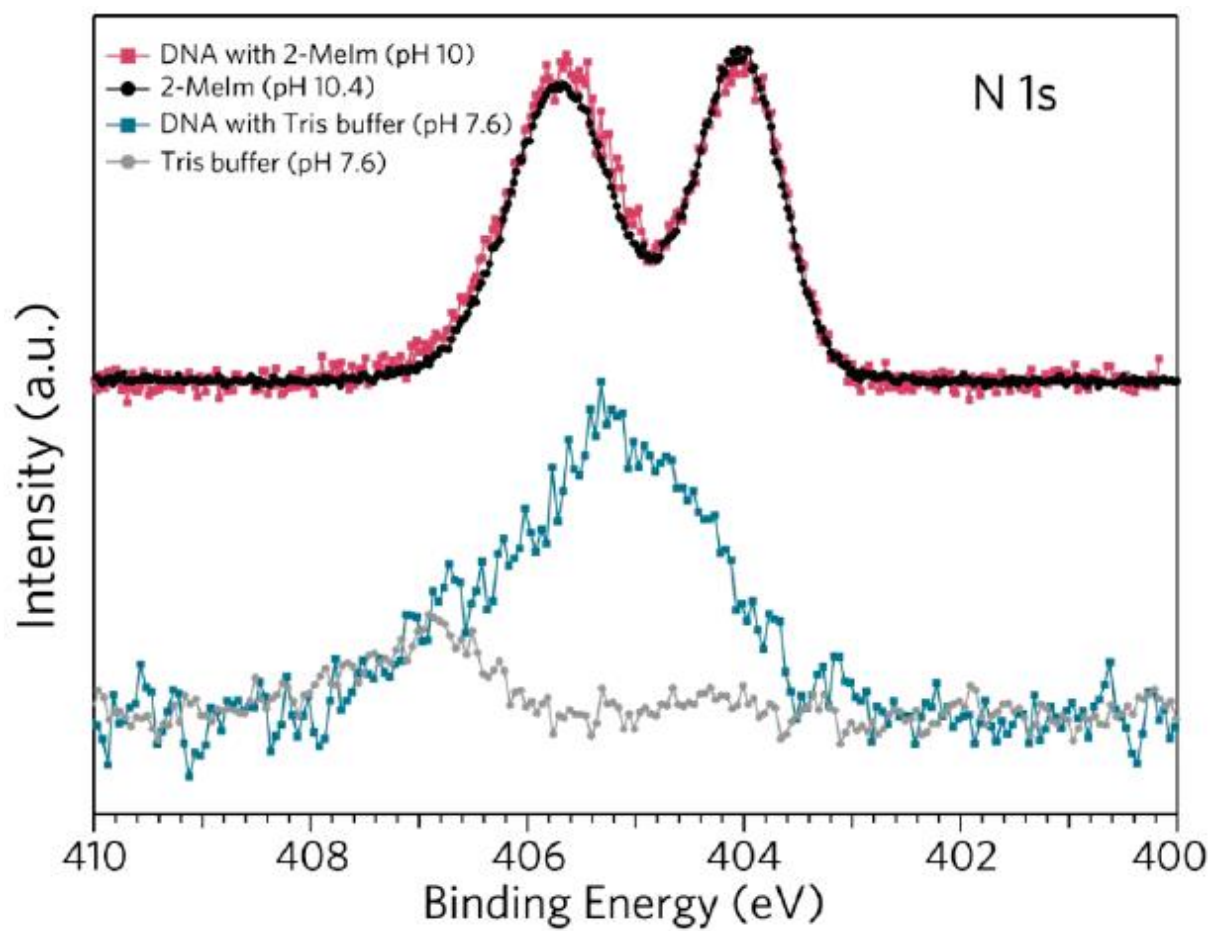


Figure S27. Liquid jet XPS of N 1s for the DNA and Melm solution mixture.

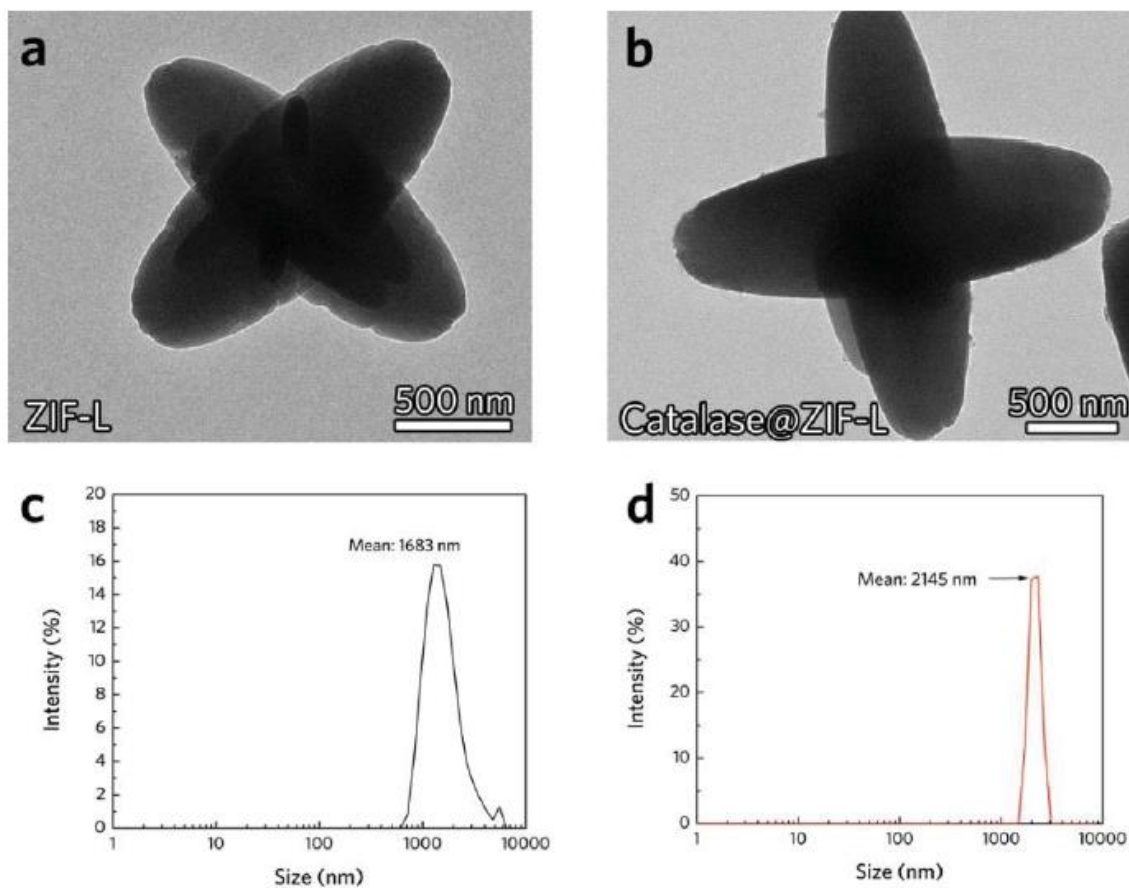


Figure S28. **Change of ZIF-L particle morphology before and after incorporating the biomolecules.** (ab) TEM images of the pure ZIF-L and catalase@ZIF-L. (c-d) DLS results of the pure ZIF-L and the catalase@ZIF-L.

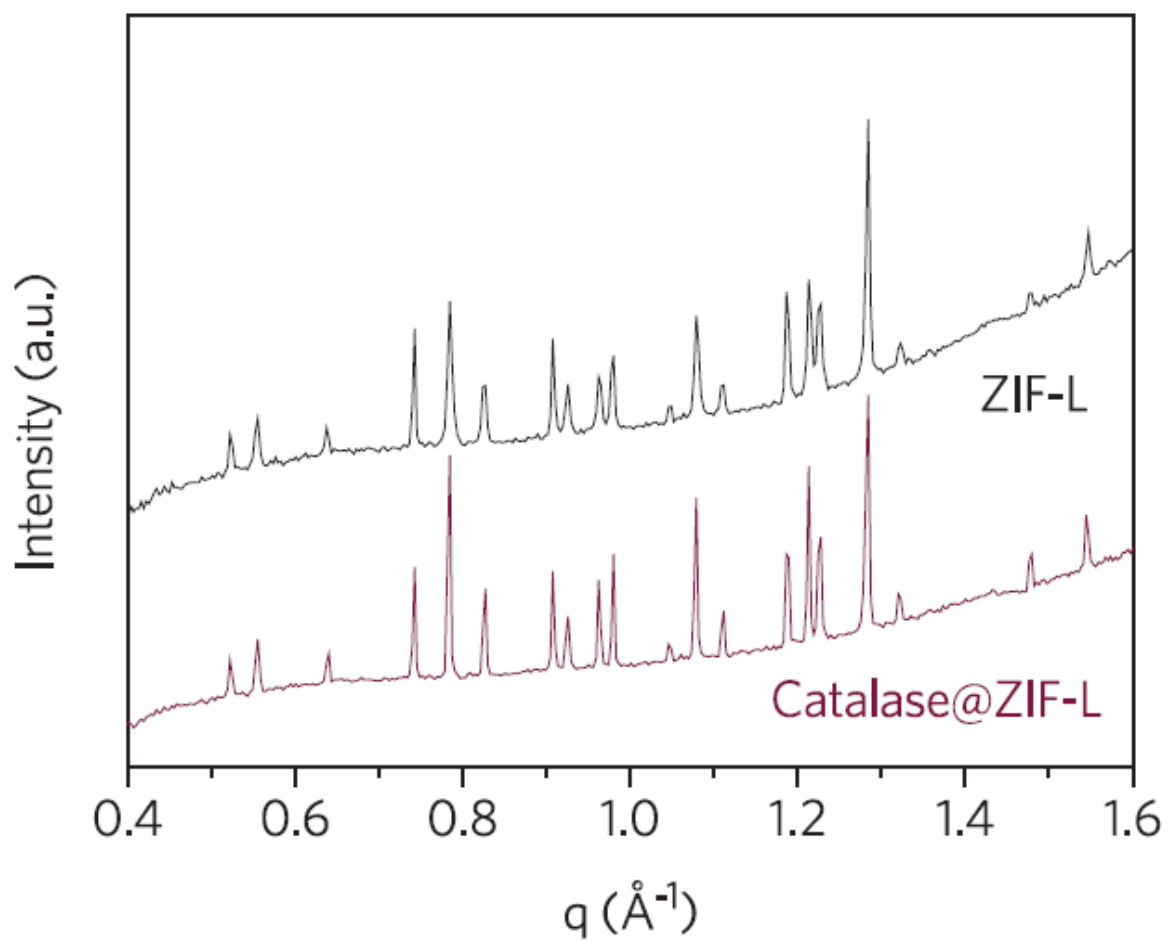


Figure S29. SAXS Crystal structure of catalase@ZIF-L and ZIF-L.

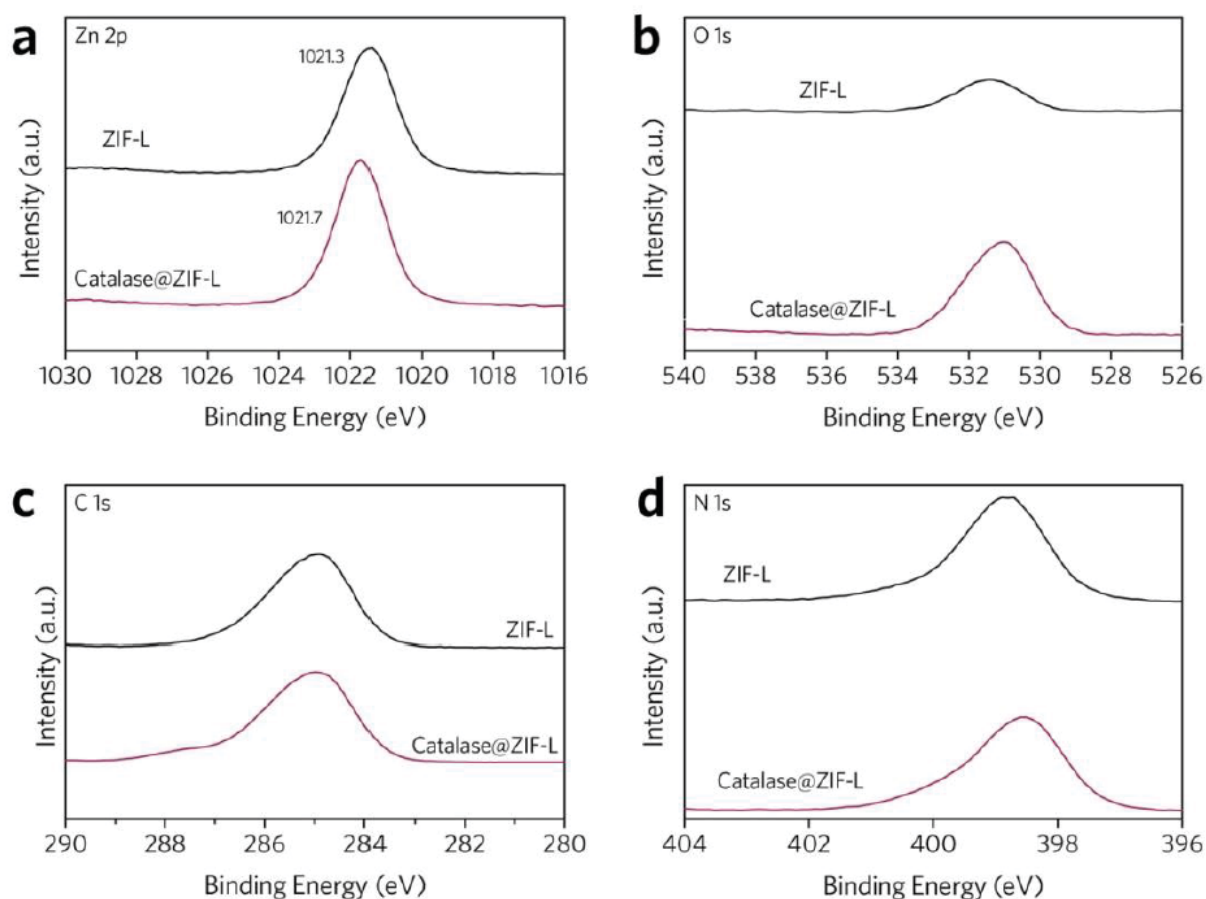


Figure S30. XPS (a) Zn 2p, (b) O 1s, (c) C 1s, and (d) N 1s spectra of the catalase@ZIF-L and pure ZIF-L. The peak shift for Zn 2p suggests the formation of new bonds between Zn and catalase. However, due to the complicated chemical environment for the protein molecules (e.g. the presence of a large amount of non-coordinating oxygen atoms), the peak shift for the O1s is less obvious.

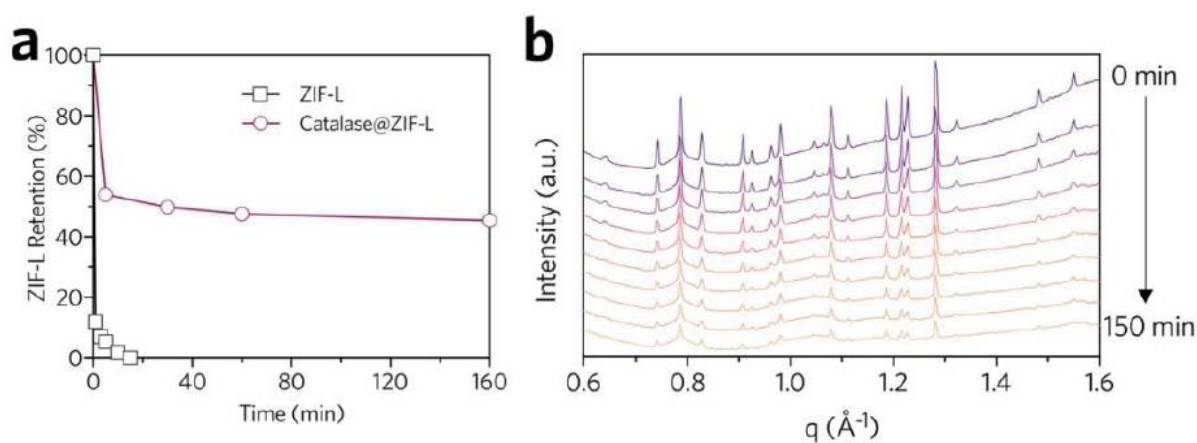


Figure S31. **Dissolution process in acid for catalase@ZIF-L.** (a) ZIF-L retention for catalase@ZIF-L and ZIF-L during the acid treatment process in acetate acid. The results are based on the dissolved Zn ion concentration in the supernatant monitored by ICP-MS. (b) *In-situ* SAXS pattern variance during the dissolution process.

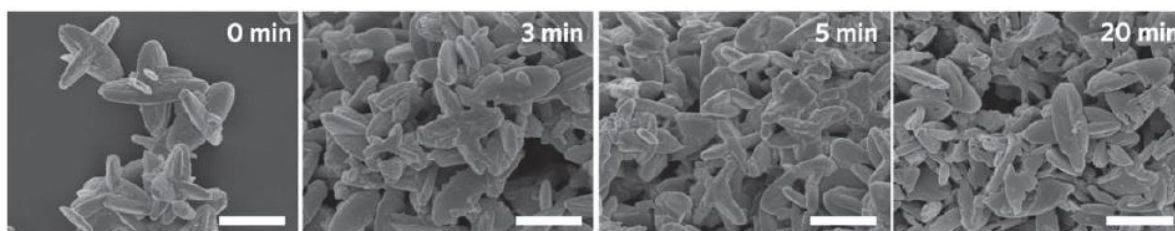


Figure S32. SEM image of the catalase@ZIF-L with different acid treatment time. Scale bars are 2 $\mu$ m.

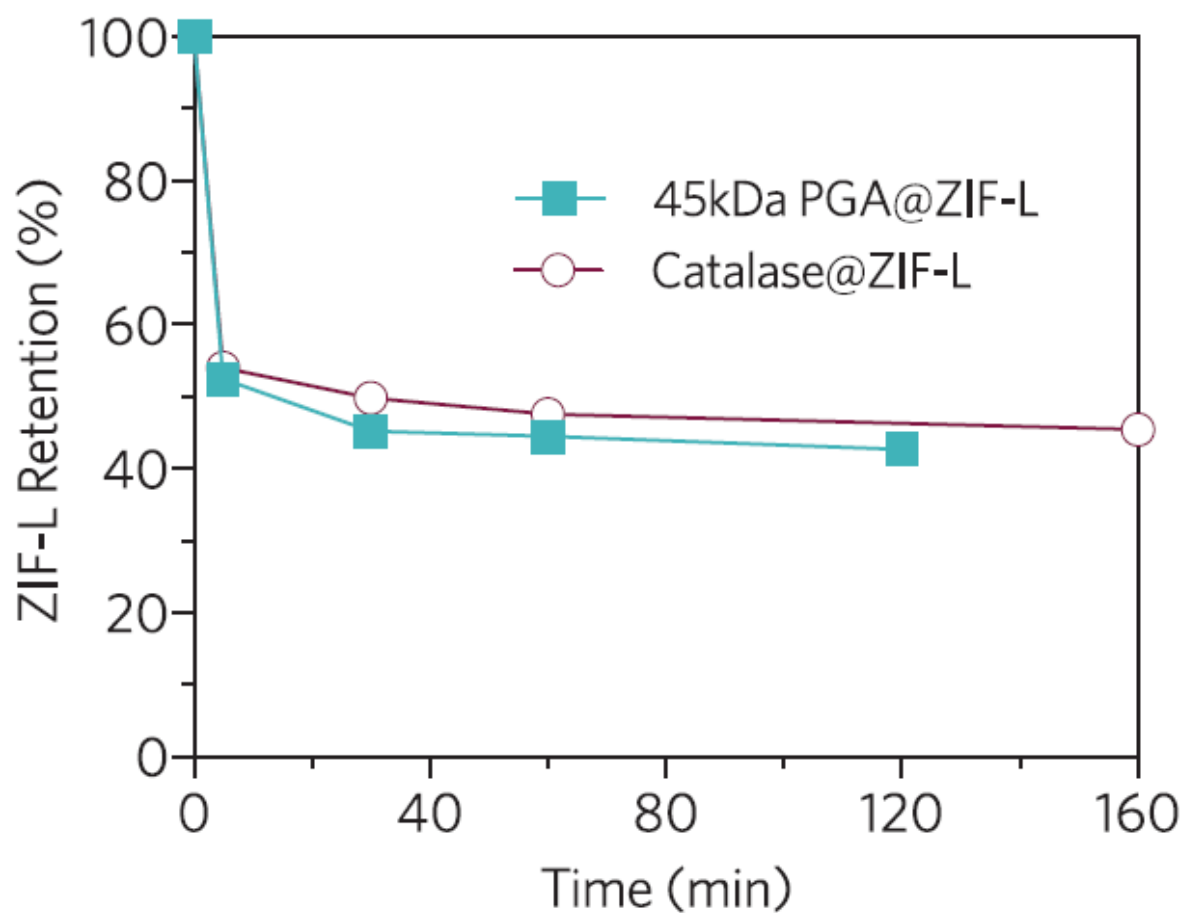


Figure S33. **Dissolution process in acid for catalase@ZIF-L and 45 kDa PGA@ZIF-L during the acid treatment process in pH 5 acetate buffer.** The results are based on the dissolved Zn ion concentration in the supernatant monitored by ICP-MS. 0.04  $\mu$ mol of catalase and PGA were applied for the initial synthesis with encapsulation efficiency higher than 98 % for the 45 kDa PGA.

## Supplemental Table Section

Table S1. Encapsulation efficiency of biomolecule@ZIFs.\*

	PGA@ZIF-L	PLL@ZIF-L	DNA@ZIF-L	Catalase@ZIF-L	PGA@ZIF-8
Encapsulation efficiency (%)	98.3%	95.6%	92.7%	96.6%	95.4%
Biomolecule weight percentage (%)	8.2%	7.9%	7.2%	8.1%	7.4%

\*Encapsulation efficiency was defined as the percentage ratio of the encapsulated biomolecule versus the originally added biomolecule in the synthesis solution.

Table S2. Refinement results via Pawley method for ZIF-L and DNA@ZIF-L. The 10-40 degree range was refined.

	a (Å)	b (Å)	c (Å)	R <sub>wp</sub>
Pure ZIF-L	24.120(2)	17.060(1)	19.737(1)	9.8
DNA@ZIF-L	24.121(5)	17.061(0)	19.738(2)	9.3
ZIF-L reference from cif ID 1509273	24.119(1)	17.060(4)	19.739(8)	N/A

Table S3. Kinetics of the free and immobilized catalase with H<sub>2</sub>O<sub>2</sub> substrate. The kinetic parameters were determined with UV-Vis colorimetric (UV) and direct visual (DV) approaches, respectively.

	K <sub>m</sub> (mM)	K <sub>cat</sub> (s <sup>-1</sup> )
Free	42.0 ± 1.5 (UV)	1010 ± 57 (UV)
	43.7 ± 2.3 (DV)	991 ± 37 (DV)
Catalase@ZIF-L	18.6 ± 2.2 (UV)	212 ± 18 (UV)
	20.3 ± 1.8 (DV)	191 ± 20 (DV)

## Supplemental Experimental Procedures

**Materials.** All chemicals were obtained commercially and used without additional purification. Zinc nitrate hexahydrate (99.0%), hydrogen peroxide (H<sub>2</sub>O<sub>2</sub>, 30.0%), 2-methylimidazole (MeIm, 99.0%), deoxyribonucleic acid (DNA, 1.3 × 10<sup>6</sup> Da, ~2,000 bp), catalase, poly-L-lysine (PLL, 70~150 kDa), poly-L-glutamic acid (PGA, 1.5-45 kDa), ethylenediaminetetraacetic acid (EDTA) were purchased from Sigma-Aldrich. Tris (hydroxymethyl) aminomethane (Tris, >99.0%), Bradford reagent sodium acetate and acetic acid were purchased from Chem Supply. All other reagents were obtained from Sigma-Aldrich without further purification.

**Computational Methodology.** DFT calculations were performed using projected augmented wave (PAW)<sup>6,7</sup> potentials as implemented in VASP code<sup>8,9</sup> with following electrons treated explicitly: Zn 3d<sub>10</sub>4s<sub>2</sub>, O 2s<sub>2</sub>2p<sub>4</sub>, C 2s<sub>2</sub>2p<sub>2</sub>, N 2s<sub>2</sub>2p<sub>3</sub> and H 1s<sub>1</sub>. Van der Waals functional (optB86b-vdW)<sup>10</sup> is used to treat exchange-correlation part. A 500 eV kinetic energy cutoff and a gamma point only k-point mesh were used for all calculations. Clusters were put at the center of a 20×40×40 Å<sup>3</sup> box and relaxed until interatomic forces were smaller than 0.01 eV/Å. PGA is aligned along a-axis (20 Å direction).

**Activity assay of catalase.** In order to examine the activity of free and encapsulated catalase, we applied two different enzymatic activity assay approaches. For the colorimetric method, 0.125 mL 2.5 wt % H<sub>2</sub>O<sub>2</sub> solution was added to 2 mL of either free or encapsulated catalase solution (pH 7, 50 mM Tris buffer), and the final concentration of the H<sub>2</sub>O<sub>2</sub> was monitored by UV-Vis spectrophotometry at 240 nm over a period of 5 min with a time interval of 20 s. Benchmark tests were also carried out to monitor the reduction of the H<sub>2</sub>O<sub>2</sub> concentration when mixed with 2 ml of 0.5 M Zn(NO<sub>3</sub>)<sub>2</sub>, 2 mg/mL ZIF-L solution or pure water, respectively. The benchmark tests showed that the variance of the UV-Vis absorbance readings over the tested time range (from 10s to 5 min) was less than 1.5 %. For the direct visual approach, 100 μL of catalase solution was mixed with 100 μL 1 % Triton X-100 solution, then the reaction was initiated with the addition of 100 μL H<sub>2</sub>O<sub>2</sub>.<sup>11</sup> The activity of catalase was calculated based on the height of the generated bubble layer (Scheme S1). The kinetic parameters of both free and immobilized catalase were examined with both activity assay approaches, with the H<sub>2</sub>O<sub>2</sub> concentration in the final reaction medium varied from 1 to 500 mM.

**Characterization.** *In-situ* Small Angle X-ray scattering (SAXS) patterns, and far-infrared (FIR)/terahertz (THz) radiation were collected at the Australian Synchrotron. The *in-situ* SAXS was investigated with SAXS beamline at 16 keV, 2675 mm camera length using a Pilatus 1M detector at transmission mode. For each analysis, a line scan of 3 mm at 0.3 mm/s was conducted. The background was subtracted. The data was processed using in-house developed Scatterbrain software for averaging and background subtraction. The FIR/THz beamline was equipped with an attenuated total reflectance (ATR) sampling accessory. The tested range was 50-750 cm<sup>-1</sup>. The spectrometer used the THz/far-infrared synchrotron beam (200 mA), with a total 240 scans.

The solid-state <sup>13</sup>C NMR experiments were carried out on Bruker AVANCE III 700 spectrometer with a 16.4 Tesla superconducting magnet operating at frequencies of 700 MHz and 175 MHz for the <sup>1</sup>H and <sup>13</sup>C nuclei respectively. The samples were center packed into 4 mm zirconia rotors fitted with a Kel-F cap. <sup>13</sup>C Cross-Polarization with Magic Angle Spinning (<sup>13</sup>C CPMAS) NMR spectra of the material was acquired at 8 kHz MAS with 2 ms of ramped cross-polarization (CP) time to transfer the coherence from the <sup>1</sup>H to the <sup>13</sup>C nuclear spins and 80 kHz <sup>1</sup>H SPINAL64 decoupling during acquisition. A 10 ms <sup>1</sup>H spin diffusion time was inserted prior to the CP, to equilibrate the <sup>1</sup>H signals between the MOF and the guest polymer. The Total Suppression of Spinning Sidebands (TOSS) with <sup>13</sup>C 180° pulse length of 7.2 μs scheme was implemented prior to acquisition to prevent any overlap of the isotropic peaks with the spinning sideband peaks. 1.5 s recycle delays were used for the measurements and 2 k transients were co-added for sufficient signal to noise. The 2D <sup>13</sup>C-<sup>1</sup>H heteronuclear correlation (HETCOR) spectra, were acquired 2k Transients in the direct (F-2) dimension and 96 increments of 60.04 μs each in the indirect (F1) dimension. Frequency Switch Lee-Goldburg homonuclear decoupling at a field strength of 95 kHz decoupling was applied during <sup>1</sup>H evolution to enable high resolution in the <sup>1</sup>H dimension. After <sup>1</sup>H evolution, a 10 ms <sup>1</sup>H spin diffusion time was employed prior to polarization transfer to the <sup>13</sup>C nuclei to ensure signal transfer from the polymer to the methylimidazole moieties. The <sup>13</sup>C chemical shifts were referenced to adamantane. For the composite samples, because the ZIF-L is crystalline and biomolecules are amorphous/disordered in addition to being relatively low in concentration, the ZIF signals are sharp while those of the polymer are very broad. In order to clearly show the biomolecule signals, the <sup>13</sup>C spectral region containing the biomolecule peaks are replotted in the insets, with a 20-fold vertical expansion, and sufficient Gaussian broadening applied to minimize the noise. \* star is the residual spinning sideband of the aromatic species after the TOSS scheme. The 2D <sup>31</sup>P{<sup>1</sup>H} HETCOR was measured on a Bruker AVANCE III 300 spectrometer with a 7 Tesla superconducting magnet operating at frequencies of 300 MHz and 121 MHz for the <sup>1</sup>H and <sup>31</sup>P nuclei respectively. The other acquisition conditions were similar as that for the <sup>13</sup>C{<sup>1</sup>H} HETCOR.

X-ray absorption fine structure spectroscopy (XAFS) measurements entailing both near edge structure (XANES) and extended fine structure (EXAFS) were performed at the BAMline (BESSY-II) at Zn-K (9659 eV) edge in transmission mode. Data evaluation: all samples were measured three times and merged in μ(E) to increase signal to noise ratio. For data analysis and evaluation, the open source software packages Athena and Artemis based on IFEFFIT was used<sup>12</sup>. For background subtraction, the Rbkg value was set to 1.0. All spectra were normalized to the post-edge region, free from absorption features. A

Hanning-type Fourier window for forward Fourier transform was set to the  $k$ -range between  $2-8 \text{ \AA}^{-1}$  with a  $dk$  value of 0.3.

Liquid microjet XPS measurements were performed with the LiquidPES and the SOL<sup>3</sup>PES setups at the U41-PGM and U49/2-PGM-1 beamlines at the BESSY II synchrotron radiation facility. Details of the setups can be found elsewhere<sup>13,14</sup>. Briefly, nitrogen 1s spectra were collected from a liquid microjet of 35  $\mu\text{m}$  diameter that was injected through a fused silica capillary into the vacuum chamber with a velocity of 30 m/s. The jet-reservoir temperature was held at 12°C. The temperature at the locus of interaction with the synchrotron light was much lower, approximately 2-5°C, due to evaporative cooling. Photoelectrons were collected with a hemispherical electron analyzer, which is mounted normal both to the liquid jet axis and the polarization axis of the incoming synchrotron light. Photon energies used were 510 eV for the DNA + 2-methylimidazole (pH = 10) and the pure 2-methylimidazole at pH = 10.4. The DNA + TRIS buffer as well as the pure TRIS buffer solution were kept at pH = 7.6 and measured at a photon energy of 480 eV. The combined energy resolution of the beamlines and the electron analyzer is better than 250 meV at these photon energies. Energy calibration was done using the 1b<sub>1</sub> HOMO peak of water as a reference, which has a binding energy of 11.31 eV with respect to vacuum<sup>15</sup>. All solutions were prepared using highly demineralized water (conductance >18 M $\Omega$ /cm<sup>-1</sup>). DNA samples investigated are from hering sperm (Sigma Aldrich #D7290).

Field-emission scanning electron microscope (SEM) and transmission electron microscope (TEM) images were taken on a Nova NanoSEM 230 and FEI Tecnai G2, respectively, under 10 kV acceleration voltage. The samples were coated using Emitech K575x Evaporative Chromium Coater before measuring. The size distribution of particles was obtained from Dynamic Light Scattering (DLS) analysis by using a Malvern Zetasizer Nano ZS instrument. Surface chemistry of the particles was obtained from the X-ray Photoelectron Spectroscopy (XPS) analysis, taken on the Thermo Scientific ESCALAB 250xi instrument with a monochromatic Al K $\alpha$  X-ray source ( $h\nu = 1486.6 \text{ eV}$ ). To remove charging effects during the measurements, a low-energy electron flood gun with proper energy was applied. All spectra were aligned to the C 1s at 284.8 eV. For fluorescence test, the biomolecules were tagged with fluorescein isothiocyanate (FITC) before encapsulation within the ZIF particles. Confocal laser scanning microscopy images were obtained on a Leica TCS SP2 inverted system. The Attenuated Total Reflectance Fourier Transform Infrared Spectroscopy (FTIR) measurement was performed by using the Bruker Alpha FTIR Spectrometer. Gas adsorption-desorption isotherm was carried out with Micromeritics ASAP 2020 analyzer. At least 100 mg sample was loaded into the sample vial and dried under vacuum for 48 h. The nitrogen adsorption was conducted at 77 K with the pressure range between 0-1 bar. The circular dichroism (CD) spectra of DNA before and after encapsulation in ZIF-L was taken between 230 and 320 nm on a Chirascan Plus CD spectrometer. The results presented represent the average of 20 spectra and are plotted as  $\Delta\epsilon$ . The measured sample volume was 0.5 mL, containing around 0.75  $\mu\text{M}$  DNA. For the DNA@ZIF-L 0.5 mL of 62.5 mM EDTA was applied to dissolve the ZIF-L to release the encapsulated DNA.

### Supplemental Reference

1. Gaur, A., Shrivastava, B.D., and Nigam, H.L. (2013). X-Ray Absorption Fine Structure (XAFS) Spectroscopy – A Review. *Proc. Indian Natn. Sci. Acad.* **79**, 921-966.
2. Bhattacharyya, S., Han, R., Kim, W.-G., Chiang, Y., Jayachandrababu, K.C., Hungerford, J.T., Dutzer, M.R., Ma, C., Walton, K.S., Sholl, D.S., *et al.* (2018). Acid Gas Stability of Zeolitic Imidazolate Frameworks: Generalized Kinetic and Thermodynamic Characteristics. *Chem. Mater.* **30**, 4089–4101.
3. Ghosh, P.S., Han, G., Erdogan, B., Rosado, O., Krovi, S.A., and Rotello, V.M. (2007). Nanoparticles Featuring Amino Acid-functionalized Side Chains as DNA Receptors. *Chem. Biol. Drug Des.* **70**, 13–18.
4. Goodman, C.M., Chari, N.S., Han, G., Hong, R., Ghosh, P., and Rotello, V.M. (2006). DNA-binding by Functionalized Gold Nanoparticles: Mechanism and Structural Requirements. *Chem. Biol. HTMLent Glyphamp Asciiamp Drug Des.* **67**, 297–304.
5. Kudsiöva, L., Arafiena, C., and Lawrence, M.J. (2008). Characterisation of Chitosan-Coated Vesicles Encapsulating DNA Suitable for Gene Delivery. *J. Pharm. Sci.* **97**, 3981–3997.
6. Kresse, G., and Joubert, D. (1999). From Ultrasoft Pseudopotentials to the Projector Augmented-Wave Method. *Phys. Rev. B* **59**, 1758–1775.
7. Blöchl, P.E. (1994). Projector Augmented-Wave Method. *Phys. Rev. B* **50**, 17953–17979.
8. Kresse, G., and Furthmüller, J. (1996). Efficiency of *ab-initio* Total Energy Calculations for Metals and Semiconductors using a Plane-wave Basis Set. *Comput. Mater. Sci.* **6**, 15–50.
9. Kresse, G., and Furthmüller, J. (1996). Efficient Iterative Schemes for *ab initio* Total-energy Calculations Using a Plane-wave Basis Set. *Phys. Rev. B* **54**, 11169–11186.
10. Klimeš, J., Bowler, D.R., and Michaelides, A. (2011). Van der Waals Density Functionals Applied to Solids. *Phys. Rev. B* **83**, 195131.

11. Iwase, T., Tajima, A., Sugimoto, S., Okuda, K., Hironaka, I., Kamata, Y., Takada, K., and Mizunoe, Y. (2013). A Simple Assay for Measuring Catalase Activity: A Visual Approach. *Sci. Rep.* **3**, 3081.
12. Ravel, B., and Newville, M. (2005). *ATHENA*, *ARTEMIS*, *HEPHAESTUS*: data analysis for X-ray absorption spectroscopy using *IFEFFIT*. *J. Synchrotron Radiat.* **12**, 537–541.
13. Seidel, R., Thürmer, S., and Winter, B. (2011). Photoelectron Spectroscopy Meets Aqueous Solution: Studies from a Vacuum Liquid Microjet. *J. Phys. Chem. Lett.* **2**, 633–641.
14. Seidel, R., Pohl, M.N., Ali, H., Winter, B., and Aziz, E.F. (2017). Advances in liquid phase soft-x-ray photoemission spectroscopy: A new experimental setup at BESSY II. *Rev. Sci. Instrum.* **88**, 073107.
15. Kurahashi, N., Karashima, S., Tang, Y., Horio, T., Abulimiti, B., Suzuki, Y.-I., Ogi, Y., Oura, M., and Suzuki, T. (2014). Photoelectron spectroscopy of aqueous solutions: Streaming potentials of NaX (X = Cl, Br, and I) solutions and electron binding energies of liquid water and X<sup>-</sup>. *J. Chem. Phys.* **140**, 174506.